REPORT DOCUMENTATION PAGE

AFRL-SR-AR-TR-06-0465

1. REPORT DATE *(DD-MM-YYYY)*

2. REPORT TYPE
FINAL REPORT

3. DATES COVERED *(From - To)*
15 May 2003 - 14 May 2006

4. TITLE AND SUBTITLE
IMPLEMENTATION OF MICROWAVE ACTIVE NULLING AND INTERROGATION OF BOUNDARY IMPEDANCE

5a. CONTRACT NUMBER

5b. GRANT NUMBER
F49620-03-C-0036

5c. PROGRAM ELEMENT NUMBER
61102F

6. AUTHOR(S)
DR. HOTON HOW

5d. PROJECT NUMBER
2304/IX

5e. TASK NUMBER
IX

5f. WORK UNIT NUMBER

7. PERFORMING ORGANIZATION NAME(S) AND ADDRESS(ES)
HOTECH INC
262 CLIFTON STREET
BELMONT MA 02478

8. PERFORMING ORGANIZATION REPORT NUMBER

9. SPONSORING/MONITORING AGENCY NAME(S) AND ADDRESS(ES)
AIR FORCE OF SCIENCTIFIC RESEARCH
AFOSR/NE
875 NORTH RANDOLPH STREET
SUITE 325 ROOM 3112
ARLINGTON VA 22203-1768
Dr. Arje Nachman

10. SPONSOR/MONITOR'S ACRONYM(S)

11. SPONSOR/MONITOR'S REPORT NUMBER(S)

12. DISTRIBUTION/AVAILABILITY STATEMENT
DISTRIBUTION STATEMENT A: UNLIMITED

13. SUPPLEMENTARY NOTES

14. ABSTRACT

Electromagnetic Interrogation over Electric Boundary -H. How and C. Vittoria, "Microwave Impedance Control Over A Ferroelectric Boundary Layer", IEEE Trans. Microwave Theory Tech., MTT-52(9), pp. 2177-2182, Sep. 2004.
Electromagnetic Interrogation over Electric Boundary -H. How and C. Vittoria, "Microwave Impedance Control Over a Ferrite Boundary Layer" IEEE Trans. Magnetics, Mag-41(3), pp. 1126-1131, 2005.
Phase Control Over Electromagnetic Signal -H. How and C. Vittoria, "Microwave Phase Shifter Utilizing Nonreciprocal Wave Propagation," IEEE Trans. Microwave Theory Tech., MTT-52(8), 2004.
Electromagnetic Interrogation involving Hexagonal Ferrite -H. How, X. Zuo, and C. Vittoria, "Wave Propagation in Ferrite Involving Planar Anisotropy - Theory and Experiment" IEEE Trans. Magnetics, Mag-41(8), pp. 2349-2355, 2005.

15. SUBJECT TERMS
MICROWAVE

16. SECURITY CLASSIFICATION OF:			17. LIMITATION OF ABSTRACT	18. NUMBER OF PAGES	19a. NAME OF RESPONSIBLE PERSON
a. REPORT	b. ABSTRACT	c. THIS PAGE			
U	U	U			19b. TELEPHONE NUMBER *(Include area code)*

FINAL REPORT

AFOSR Contract F49620-03-C-0036

"Implementation of Microwave Active Nulling and Interrogation of Boundary Impedance"

Hotech, Inc.
phone: (617)720-3968, fax: (617)720-3968
email: HHOW@HOTECH.COM

RESEARCH ACCOMPLISHED

- Electromagnetic Interrogation over Electric Boundary
  - H. How and C. Vittoria, "Microwave Impedance Control Over A Ferroelectric Boundary Layer", IEEE Trans. Microwave Theory Tech., MTT-52(9), pp.2177-2182, Sept. 2004.
- Electromagnetic Interrogation over Magnetic Boundary
  - H. How and C. Vittoria, "Microwave Impedance Control Over a Ferrite Boundary Layer" IEEE Trans. Magnetics, Mag-41(3), pp.1126-1131, 2005.
- Phase Control Over Electromagnetic Signal
  - H. How and C. Vittoria, "Microwave Phase Shifter Utilizing Nonreciprocal Wave Propagation," IEEE Trans. Microwave Theory Tech., MTT-52(8), 2004.
- Electromagnetic Interrogation involving Hexagonal Ferrite
  - H. How, X. Zuo, and C. Vittoria, "Wave Propagation in Ferrite Involving Planar Anisotropy —Theory and Experiment" IEEE Trans. Magnetics, Mag-41(8), pp.2349-2355, 2005.

BACKGROUND

Microwave and millimeter-wave (MMW) devices and systems are becoming increasingly important today for both defense and commercial applications. For example, in the collision avoidance industries, low-profile antennas are needed which provide electronically steerable radiations to detect and identify obstacles and intrusions in front of a moving vehicle. Upon navigation the receiver antennas need to follow and trace the motion of GPS (Global Positioning Systems) satellites so as to continuously monitor and update their positions. Also, there is a need to create radiation nulls along certain spatial directions for an antenna transmitter/receiver antenna to warrant secure and covert communications. Impedance control over boundary layers is required so that the synthesized surface impedance give insignificant reflection along an interrogation direction. Other applications can be found in target searching/tracking radars, satellite communication systems, and TV program broadcasting antennas installed with a civilian jet carrier.

In a phased array system it is possible to include frequency-agile materials (varactors, ferroelectrics, and ferrites) to tune and adjust the phase and amplitude of each individual element so as to compose and tailor the overall radiation into a desirable pattern. However, beam forming in this manner is expensive; depending on the speed, frequency, and angle of steering, each phase-shift element can cost as much as $1,000, and in a system containing 10,000 elements, the price of the antenna array system can be formidable. Power dissipation is another consideration, since amplifiers are used following each of the phase shifting processes to compensate signal propagation loss, or insertion loss. To avoid overheating, water cooling is, therefore, often required in a large phased array system. Isolators are used to minimize internal reflections.

A radiation beam can also be steered via mechanical means, as commonly observed for a traffic-control radar installed at the airports. However, steering in this manner is slow, suffering from potential mechanical worn-out and breakdown. To incorporate free rotation, the antenna take up considerable space and the shape of the antenna is not conformal. As such, it is unlikely to apply a mechanically rotating radar in a body moving at high speed.

A reflector-array antenna operates in the same manner as an optical grating device: The reflected beam is constructed coherently from each of the array elements according to its reflection phase and electric path [Berry, D.G., et al, IEEE Transaction Antennas and Propagation, vol.11, pp.645-651, 1963]. Therefore, by adjusting the phase and/or electric path of the reflecting elements the overall beam construction can be controlled and manipulated, not only in its reflection directions, but also in its geometric shape characteristic of, for example, beam width, side-lobe locations, and nulling directions.

The impedance of an active reflector surface can be varied so that upon interrogation it can assume an arbitrary value. The surface impedance is subject to electronic tuning in two dimensions, allowing both of its real part and imaginary part to change, simultaneously and independently. In other words it needs to adjust two parameters to completely control the surface impedance, which may be taken as the permittivity and the permeability of the surface layer of the reflector, for example. As such, ferroelectric and ferrite materials are included with the reflector surface, and electric voltage and magnetic field are applied to change the permittivity and the permeability of the surface layer respectively thereby changing the surface impedance of the reflector electronically in two dimensions.

Electronic switches are used on the surface of the reflector to form a phase-switched screen (PSS) so as to effectively minimize reflection over a broadened bandwidth (B. Chambers and A. Tennant, IEEE Antennas and Propagation Magazine, Vol.46(6), pp.23-37, 2004). Furthermore, in-situ phase-shift elements are deployed in local positions to facilitate convenient phase-tuning operations. For this research program the combined geometry of an active-passive reflector antenna is proposed, capable of electronically configuring its local surface impedances giving rise to beam-steering/beam-forming/beam-nulling functions in two dimensions. No amplifiers are required and hence the problem of power dissipation is minimized. Also, isolators are not used and the reflector circuit is simplified. The reflector has a low profile containing no parts on mechanical rotation. The response time is fast and the fabrication is inexpensive.

ELECTROMAGNETIC INTERROGATION OVER ELECTRIC BOUNDARY

We have successfully accomplished the research goals set up in the proposal of the program relating to implementation of microwave active nulling. In order to actively manipulate a radiation beam so as to create microwave nulling a reflector surface is deployed upon which the reflection amplitude and phase of the incident wave can be controlled via electronic means. To do this both the local impedance and phase at various spots of the reflector surface are subject to electronic tuning by imposing a bias voltage and/or a bias current, for example. This allows the local permittivity and permeability of the reflector surface to vary, respectively. Frequency agile materials such as ferroelectric and ferrites are thus needed, and only if both of the ferroelectric and ferrite materials are utilized can the local permittivity and permeability of the reflector surface be simultaneously and independently adjusted.

In performing electronic-tuning functions resonant structures are utilized to enhance sensitivities in operation. Resonance can be extrinsic or intrinsic in nature, such as dimensional resonance or ferromagnetic resonance (FMR), respectively. Therefore, the bias voltage and the bias current are distinguished in two parts. Permanent biases are referred to those bias fields providing constant global background values to bring about the necessary resonant conditions, thereby facilitating the tuning operation. Superimposed with the background biases local variable fields are thereof imposed capable of modifying the background values in small scales at ease. This warrants high-speed operation. A magnetic background bias can be achieved by using a permanent magnet generating a sufficient magnetic field over a wide area with uniformity. Helmholtz coils are then used to induce local variable changes in the overall magnetic bias field. An electric background bias can be realized via the use of a constant voltage supply, and local fields are then added to the background field using variable voltage sources to fine tune the overall electric bias field.

In order not to interfere with the RF properties of the reflector circuit DC bias electrodes are included with the resonance structure in a manner invisible to microwave propagation. That is, the bias electrode are made of thin conductor layers whose thickness compares negligibly small to the skin depth in the conductor. As such, high DC voltage up to 1000 V has been successfully expressed onto the reflector surface inducing sufficient change in permittivity. Furthermore, no soldering is required by the DC bias circuit and the bias electrodes are pressed against the resonator container walls in a straightforward manner. The employed bias electrode was cut from a commercial resistive sheet containing a gold layer of thickness 900 A deposited on top of a mylar layer.

Universal instrumentation has been fabricated allowing both the permittivity and the permeability measurements to be performed using the same equipment. Measurement instrumentation includes a coax-cable resonator whose boundary layer consists of frequency-agile materials, such as ferroelectric and ferrites. Electrodes and coils, which are required to generate the bias electric field and the bias magnetic field, respectively, are included with the measurement instrumentation, thereby causing the electronic properties of the boundary layer to change. Permanent magnet is also included so as to supply a magnetic bias background. The reason that a coax-cable resonator was chosen as the research candidate is that a coax cable supports TEM mode propagation of electromagnetic waves. This simulate the real situation, since a microwave reflector is normally used to receive the radiation waves in the far-field regime.

Two kinds of ferroelectric materials were used in measuring the permittivity changes induced in the boundary layer of the fabricated coax-cable resonator. They were both BST samples ($Ba_xSr_{1-x}TiO_3$: $x = 0.5$) obtained from Army Research Laboratory, Adelphi, MD, and from NZ Technology, Woburn, MA. While the Army sample is bulk BST of thickness 0.017", NZ sample is single crystal BST of thickness 0.4 μm grown on crystal $LaAlO_3$ substrate whose thickness is 0.02" and dielectric constant 10. Magnetic permeability measurements were performed with respect to garnet samples, G475 and G1010, which were purchased from Trans Tech, Adamstown, MD. The reflection data from the cavity resonator were analyzed rigorously. That is, instead of imposing the first order perturbation theory assuming the thickness of the included frequency agile material at the boundary layer is small, we have applied the transmission-line theory to explicitly calculate the effective thicknesses of the boundary layer. We note that the perturbation theory fails if a dielectric/magnetic sample is placed near an/a electric/magnetic wall, and explicit calculations must be applied to consider high-order effects. This is because, near an/a electric/magnetic wall electric/magnetic field vanishes, thereby invalidating the first-order expressions.

Traditionally, the measured reflection data from a resonator are analyzed with respect to a single resonance mode, assuming that mode does not couple to the other modes. In contrast we have analyzed the reflection data treating the whole spectrum of excited modes as a whole. It is necessary, because we found that the intrinsic resonance modes from the resonator couple to the other extrinsic modes forming standing modes inside the resonator. For example, at some frequencies standing modes are found in association with the boundary layer whose presence shifts considerably the resonance modes of the resonator. By plotting the measured resonance frequencies as a function of the modal number of the resonator, the shift in resonance frequencies can thus be visualized. The intrinsic modes of the resonator can thus be analyzed using interpolation, removing effectively the coupling effects due to the other extrinsic standing modes.

The measured dielectric constant for the Army samples was 330, and for the NZ samples it was 10.8. The measured fractional changes in permittivity was +0.3 for the Army samples and -0.1 for the NZ samples upon the application of a DC bias voltage of 600V and 800V, respectively. For magnetic samples we found that permeability changed significantly when FMR conditions were approached. Our calculations compared nicely with measurements.

In the past a boundary layer were studied indirectly, whose electronic properties were inferred via analyzing the measured reflection data from a resonator containing the layer as the boundary wall. There is a need to directly measure the electronic properties of the boundary layer. For example, in the RF interrogation process the electronic properties of the boundary layer are directly accessed, not involving a structural resonator in mediation. Also, there is need to analyze the loss behavior of the boundary layer, as well as its effects in influencing the reflection data from a resonator. For these purposes TRL calibration techniques need to be employed along with the reflection measurements, excluding the unwanted effects of the coupling connectors from the scattering-parameter data, for example. Furthermore, the orchestral effects due to a ferroelectric layer and a ferrite layer applied concurrently in a boundary layer needs to be investigated, exploring the profound coupling of one material in interaction with the other, and vise versa. All of these important issues will be pursued in this continuation research program.

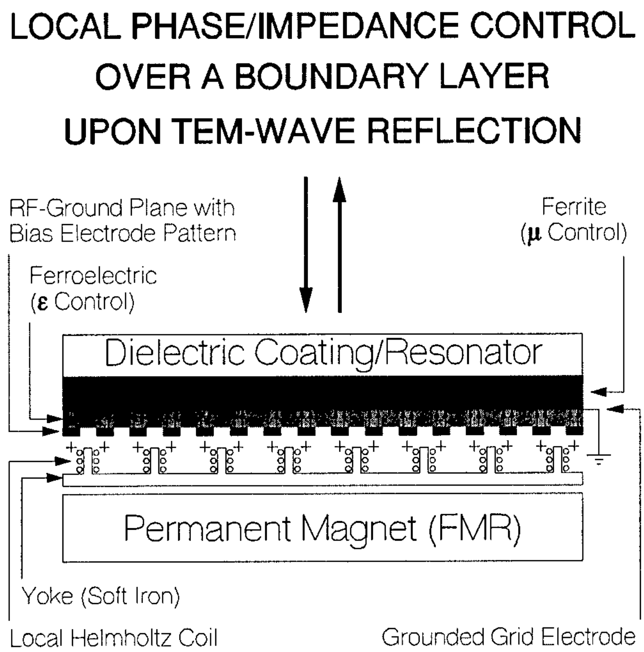

Fig.1 Configuration of an active reflector.

Fig.1 shows the configuration of an active reflector. In Fig.1 microwave radiation is incident upon the reflector, which contains a ferrite layer (purple color) and a ferroelectric layer (orange color) as constituents. The permanent magnet provides a common magnetic bias so that the FMR conditions can be readily approached, thereby facilitating sensitive magnetic tuning. Dielectric Coating layer serves as a dimensional resonator to further assist the tuning sensitivity. Electric bias is applied via a thin electrode (yellow color) whose thickness comparing negligibly small to the skin depth in the conductor. As such, microwave radiation penetrates across this thin electrode with little attenuation, arriving at a patterned RF ground plane which also serves as the positive electrode for the DC bias. As such, the permittivity ϵ of the ferroelectric layer can be electronically tuned in local areas. Helmholtz coils, which wind around a common soft-iron yoke, are used to provide local tuning in the permeability μ of the ferrite layer. As a result, the local impedance of the reflector surface can be tuned in two dimensions, independently and simultaneously.

Fig.2 shows schematically the fabricated measurement apparatus of an active reflector under electric bias. In order to simulate the far-field radiations received by a microwave reflector deployed in true situations measurements are carried out in a coax cable supporting TEM-mode wave propagation. The apparatus includes a grid electrode upon which positive voltages can be applied biasing onto the donut-shaped ferroelectric sample inducing permittivity changing. The terminology "grid electrode"

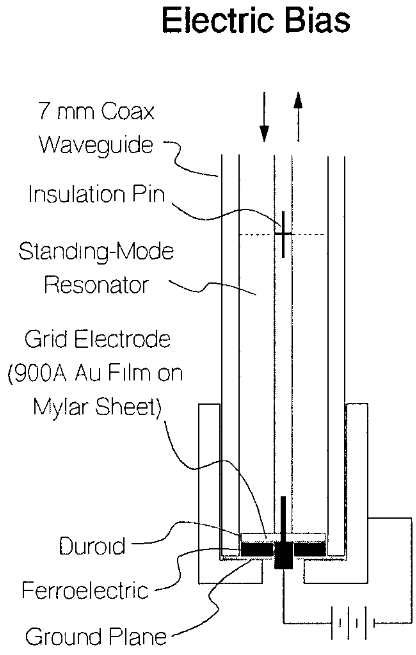

Fig.2 Measurement apparatus of an active reflector under electric bias

is used in analogy to the grid electrode in an electron vacuum-tube: it allows bias voltages to be applied without necessarily blocking the flow of an electron beam. The grid electrode of Fig.2 consists of a gold layer of thickness 900A deposited on a mylar layer. Therefore, the grid electrode in Fig.2 is so thin that electromagnetic waves can penetrate through it without experiencing much attenuation. The ferroelectric sample is shown in red color in Fig.2, and the grid electrode is shown in yellow color. The RF ground plane, which is shown in light-green color in Fig.2, serves also as the negative-voltage electrode for the DC bias. A pin insulator, which is shown in purple color, is shown in Fig.2 enabling electric isolation for the applied DC bias voltage; otherwise the DC high voltage will conduct into the network analyzer during reflection measurements, thereby causing damage to the equipment. The pin insulation also forms a cavity resonator in the coax cable, which plays the role of the dielectric coating/resonator shown in Fig.1. Note that in Fig.2 the DC bias is applied by pressing the electrodes against coax cable conductors, central conductor and outer-wall conductor, none of which require soldering contacts, and hence it is convenient to apply. A photo picture of the fabricated measurement apparatus is shown in Fig.3. In Fig.3 the home-made high voltage supply is able to provide a bias voltage up to 1250 V, whose magnitude can be adjusted by turning two knobs in Fig.3 for coarse control (left) and for fine control (right), respectively.

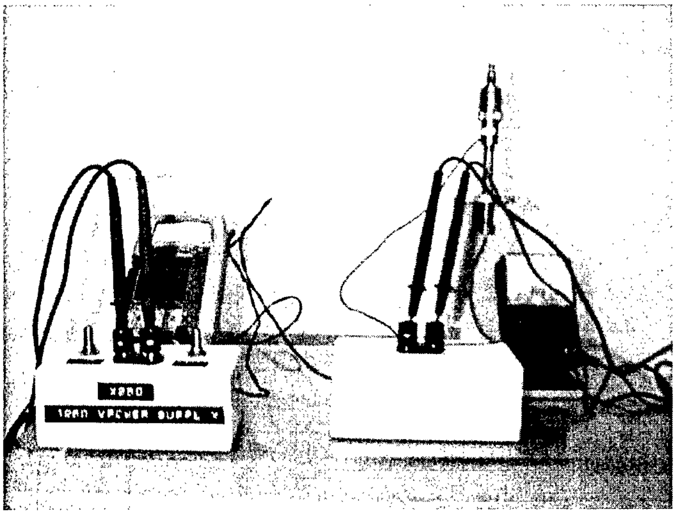

Fig.3 Fabricated measurement apparatus of an active reflector under electric bias. The home-made high-voltage supply is shown with annotation.

Instead of using the first-order perturbation theory we have developed the rigorous analytical expression for the effective thickness of a sample layer placed inside a microwave cavity resonator. That is, when the sample layer is placed in the cavity resonator, the effective thickness of the layer changes, resulting in shift of the resonant frequencies of the resonator. Therefore, by measuring the shift in resonant frequencies of the resonator electronic properties of the sample layer, such as permittivity and permeability, can be ascertained. The rigorous

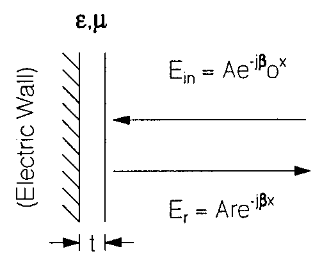

$$r = \frac{z-1}{z+1} = \frac{\cos\beta t - jz\sin\beta t}{\cos\beta t + jz\sin\beta t} = -\exp(-2j\beta_0 t_{eff})$$

$$z = (\mu/\varepsilon)^{1/2};\ \beta_0 = \omega/c;\ \beta = \beta_0(\varepsilon\mu)^{1/2}$$

Perturbation Theory ($\beta t << 1$):

$t_{eff} = t\mu$, if material backed up by an electric wall

($t_{eff} = t\varepsilon$, if material backed up by a magnetic wall)

Fig.4 Rigorous theory solving the effective thick-ness of a sample layer placed inside a cavity resoator.

formulation was developed using the transmission-line theory, since a coax-cable resonator supports TEM-mode wave propagation. In Fig.4 the sample layer is assumed to be placed near the boundary of the resonator where electric-wall boundary conditions are assumed. Similar expressions can be derived if the sample layer is placed elsewhere inside the cavity resonator. The reflection coefficient from the sample layer is set equal to the phase shift resulting from a traveling path whose length is twice the effective thickness of the sample layer. Under first-order perturbation, the mean-field theory results, and the effective thickness of the sample is weighted respectively by its permeability or permittivity value if electric-wall or magnetic-wall boundary conditions are assumed at the other side of the sample layer, please see Fig.4. We note that for the past measurements the electric-wall boundary conditions were assumed and the perturbation theory failed to provide an answer for ferroelectric samples, since the first-order shift in the resonant frequencies of the resonator vanishes when a dielectric/ferroelectric sample is placed near a RF ground plane. Near a RF ground plane the tangential component of the electric field is zero as required by the boundary conditions. A rigorous theory is thus needed at least when dealing with dielectric/ferroelctric samples. We have used the rigorous formulation shown in Fig.4 to analyze the measured reflection data from the fabricated cavity resonator for both the ferroelectric and ferrite samples.

Fig.5 shows the measured spectra of resonant frequencies of the resonator when the Army sample, ARL, Adelphi, MD (one piece or two pieces), was inserted near the RF ground plane, please see Fig.2. Instead of measuring

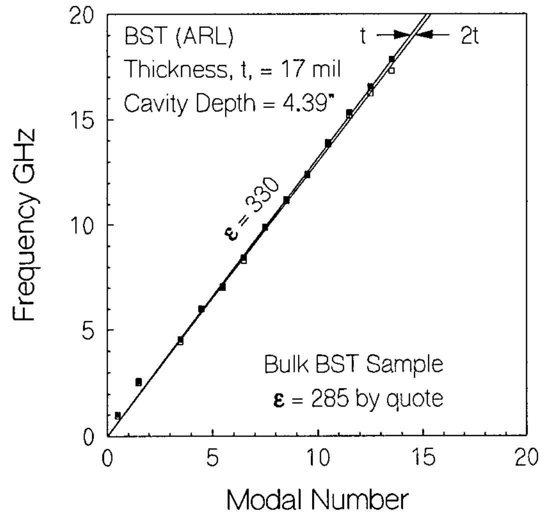

Fig.5 Resonant frequencies of the cavity resonator containing one/two piece(s) of Army BST sample.

and analyzing a single isolated resonant mode, as adopted by a traditional analysis, we have chosen to analyze the whole set of spectrum of the resonant modes to resolve uncertainties, if any, associated with these modes. The reason for doing this is that a single resonant mode may couple to the other extrinsic modes existent in the cavity resonator. For example, as will be discussed shortly, standing modes were found to be excited within a ferrite sample of a sufficient thickness, and the measured resonant frequency of the resonator is thus not its intrinsic value. As such, erroneous answer can result if care is not taken. However, if the whole set of the spectrum of the resonant modes are analyzed instead this coupling effect due to external modes can be removed by interpolation, thereby furnishing a better accuracy.

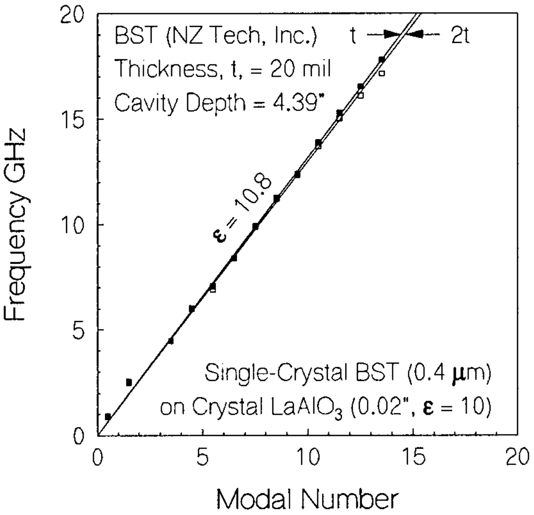

Fig.6 Resonant frequencies of the cavity resonator containing one/two piece(s) of NZ BST sample.

By interpolating the measured resonant frequencies the effective thickness of the sample layer inserted inside the resonator can thus be determined, which, in turn, gives rise to the permittivity and/or the permeability of the sample layer. Fig.6 shows two straight lines interpolated from the measured resonant frequencies of the resonator inside which one piece and two pieces of the Army sample was inserted, respectively, which is bulk BST ($Ba_xSr_{1-x}TiO_3$: x = 0.5) of a thickness 0.017". From both of the slopes of the two interpolated straight lines shown in Fig.5 the calculated permittivity of the Army sample was 330, which compared closely to its quoted value of 285. When a bias voltage of 600V was applied across the two bias electrodes, the grid electrode and the ground plane shown in Fig.2, the permittivity of the BST sample changed, and the fractional change in permittivity was determined to be -0.3; please see our Final Report for complete data exhibition and discussion. Analogously, the resonant frequencies associated with one piece and two pieces of the NZ sample are shown in Fig.6. The NZ sample consists of a single crystal BST ($Ba_xSr_{1-x}TiO_3$: x = 0.5) film of thickness 0.4 μm grown on top of a $LaAlO_3$ substrate whose thickness was 0.02" and dielectric constant was 10. From the two interpolated straight lines in Fig.6 the permittivity of the NZ sample was determined to be 10.8, which compared nicely with its quoted value of 10.6. When a bias voltage of 800V was applied, the shifts in resonant frequencies determined the fractional change in permittivity of the NZ sample to be 0.1; please refer to our Final Report for complete data exhibition and discussion. From Figs.5 and 6, we see that although the shift in resonant frequencies are small upon the application of a bias voltage, nevertheless, the developed formulation utilizing the transmission-line theory is effective in analyzing the measured reflection data from the fabricated coax-cable cavity resonator loaded with the Army and the NZ BST samples.

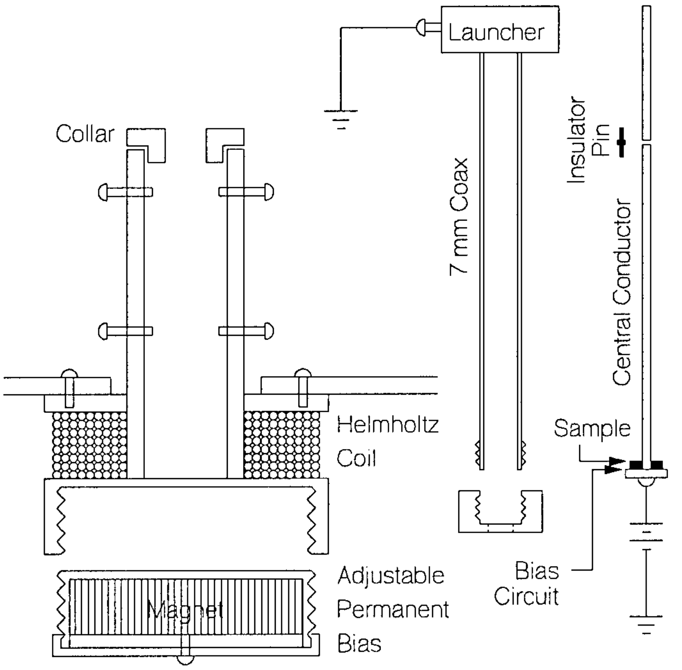

Fig.7 Schematic of the fabricated measurement apparatus under magnetic bias.

Fig.7 depicts the fabricated measurement apparatus of an active reflector under magnetic bias. The apparatus includes a permanent magnet which was able to provide a constant background magnetic field up to 3365 Oe in the ferrite sample region. Helmholtz coil was also included with the measurement apparatus which was capable of generating a variable bias magnetic field up to ±230Oe in the magnetic sample region, i.e., the maximum bias current in the Helmholtz coil was 4A. The apparatus shown in Fig.7 can also be used to supply an electric bias, although only magnetic biases were exercised for the past measurements. An insulation pin was inserted with the central conductor of the coax cable so as to electrically insulate the applied electric bias voltage. A cavity resonator was formed with the coax cable transmission line, whose role is in analogy to the dielectric coating/resonator shown in Fig.2. A photo picture of the fabricated measurement apparatus under magnetic bias is shown in Fig.8.

Fig.9 plots the measured resonant frequencies as a function of the modal number of the cavity resonator, and the resonator was loaded with a ferrite sample G475 under zero magnetic bias. The ferrite sample G475 was purchased from Trans Tech with the following parameters: $4\pi M_s = 475$ G, $\epsilon = 14.1$, $\Delta H = 200$ Oe. The ferrite sample was cut into a ring geometry of ID = 3 mm, OD = 7 mm, and thickness = 0.15". In Fig.9 it is seen that two extra modes appear near the modal number 7.5. These two extra modes were determined to be associated with the standing modes excited within the ferrite sample itself, namely, the $\lambda/2$ resonance. However, in contrast to a dielectric sample, the degeneracy between the two standing modes with opposite senses in circular polarization was removed by the internal field of the ferrite sample, and the splitting between these two

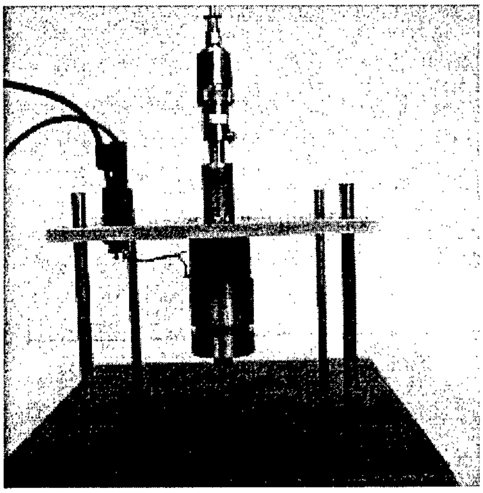

Fig.8 Photo picture of the fabricated measurement apparatus under magnetic bias.

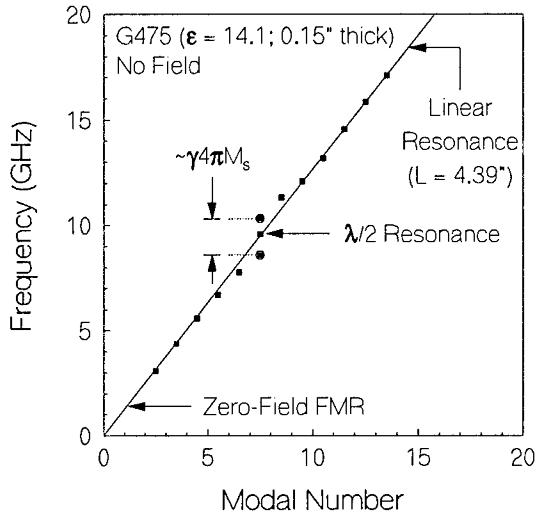

Fig.9 Measured resonant frequencies plotted as a function of the modal number.

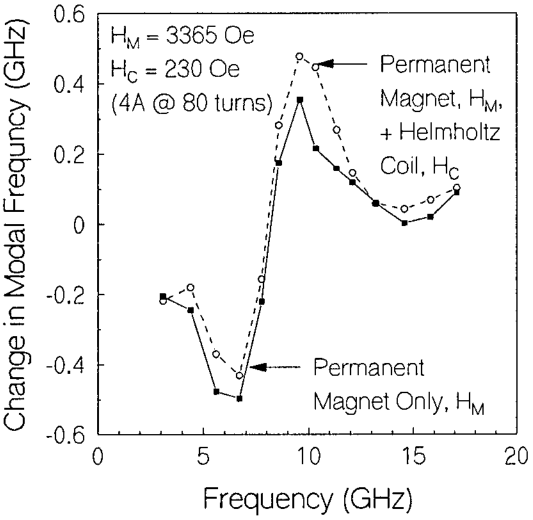

Fig.10 Measured frequency changes when the ferrite sample is applied under magnetic bias.

circularly polarized modes is roughly $\gamma 4\pi M_s$, where γ denotes the gyromagnetic ratio. In Fig.9 it is seen that the $\lambda/2$ standing modes excited within the ferrite sample couple strongly to the resonant modes of the coax-cable cavity resonator, causing the latter to shift significantly for modal numbers near 7.5. However, as mentioned previously, by interpolating the measured resonant frequencies of the coax-cable resonator, this coupling effect can be effectively removed, and the effective thickness of the inserted ferrite sample can thus be determined using the developed transmission-line theory, please see Fig.4.

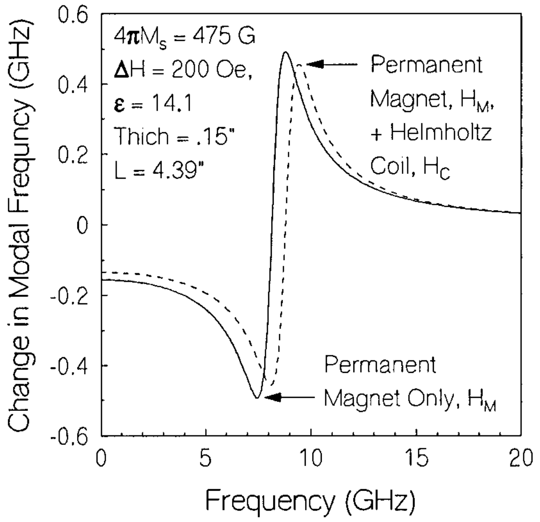

Fig.11 Calculated frequency changes when the ferrite sample is applied under magnetic bias.

Fig.10 plots the frequency changes in the resonant modes of the cavity resonator subject to magnetic biases. In Fig.10 the solid line is associated with the bias under the permanent magnet only and the dashed line under the permanent magnet plus the Helmholtz coil. Compared to electric bias applied to a ferroelectric sample, magnetic bias applied to a ferrite sample was more sensitive, giving rise to more pronounced changes in the resonant frequencies of the cavity resonator. This is

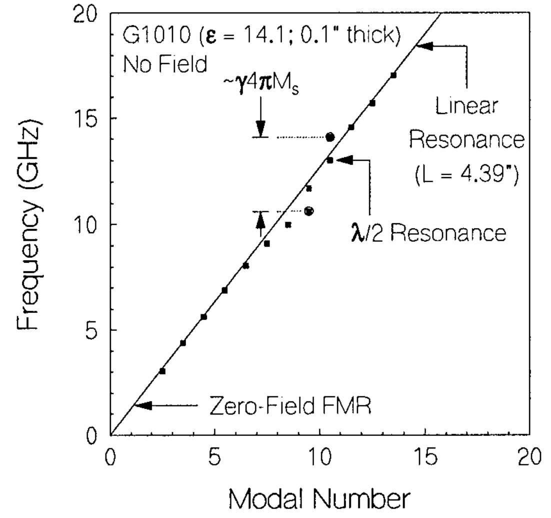

Fig.12 Measured resonant frequencies plotted as a function of the modal number.

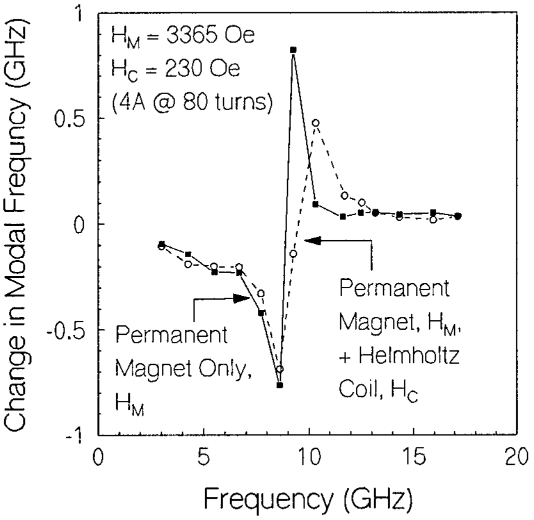

Fig.13 Measured frequency changes when the ferrite sample is applied under magnetic bias.

because both of the samples were placed near the RF ground plane of the resonator producing a maximum tangential magnetic field but a negligible tangential electric field in the sample region.

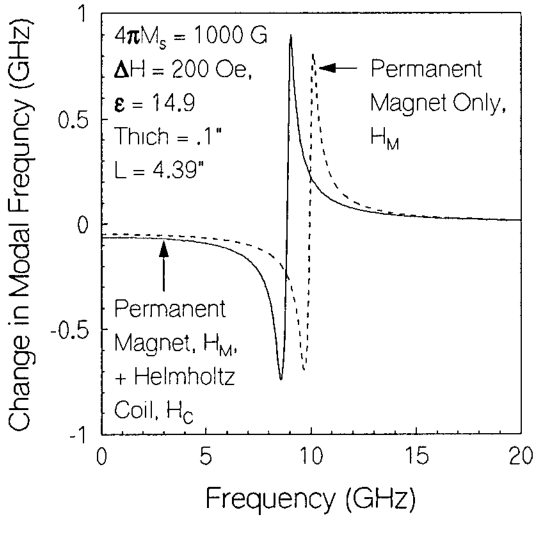

Fig.14 Calculated frequency changes when the ferrite sample is applied under magnetic bias.

Fig.11 shows the calculated frequency changes when the ferrite sample G475 was placed inside the cavity resonator subject to magnetic bias: the solid line corresponds to bias under the permanent magnet only and the dashed line under the permanent magnet plus the Helmholtz coil. We note that in deriving these curves shown in Fig.11 no adjustable parameters were used in the calculations, and the permeability of the ferrite sample was assumed to be

$$\mu_{eff} = \frac{\mu_+ + \mu_-}{2} = 1 + \frac{4\pi M_s H_{in}}{(4\pi M_s)^2 - (f/\gamma)^2}$$

Here μ_+ and μ_- are permeability of Faraday modes characteristic of wave propagation along the applied field direction with left-hand and right-hand circular polarizations in ferrites, respectively, and H_{in} is the internal field within the ferrite sample. Assuming the demagnetizing factor of the ferrite sample is close to 1, H_{in} relates to the

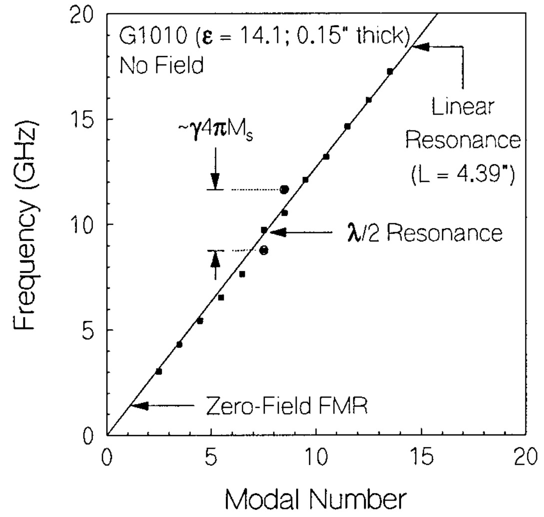

Fig.15 Measured resonant frequencies plotted as a function of the modal number.

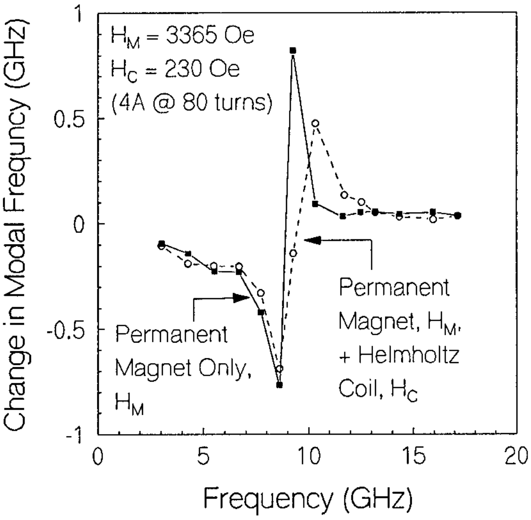

Fig.16 Measured frequency changes when the ferrite sample is applied under magnetic bias.

applied field H_a by the following equation: $H_{in} \approx H_a - 4\pi M_s$.

Comparing Fig.11 with Fig.10 we note that the agreement between theory and experiments is remarkable.

Fig.12 plots the measured resonant frequencies of the cavity resonator as a function of the modal number in the absence of a bias magnetic field. For the measurements associated with Fig.12 the cavity resonator was loaded with a ferrite sample G1010 purchased from Trans Tech. The ferrite sample was of a ring geometry characterized by the following parameters: $4\pi M_s = 1000$ G, $\epsilon = 14.8$, $\Delta H = 200$ Oe, ID = 3 mm, OD = 7 mm, and thickness = 0.1". In Fig.12 two additional standing modes appeared near modal number 9.5 and 10.5, corresponding to the λ/2 resonance in the ferrite sample itself. However, when comparing to Fig.9 showing the same standing modes in a ferrite sample with a smaller $4\pi M_s$ and a larger thickness, the standing modes in Fig.12 shift to higher frequencies with larger mode splitting in frequencies, as expected. Fig.13 shows the

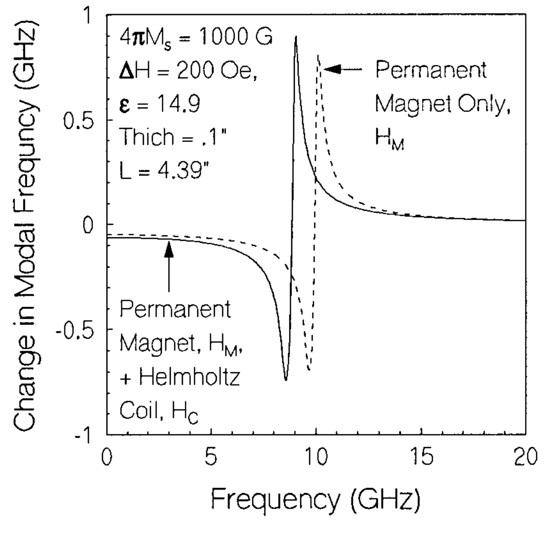

Fig.17 Calculated frequency changes when the ferrite sample is applied under magnetic bias.

frequency changes when the ferrite sample G1010 was applied under magnetic bias, and the solid curve correspond to the bias under the permanent magnet only and the dashed curve under the permanent magnet plus the Helmholtz coil. The corresponding curves from calculations are shown in Fig.14. Fig.15 shows measurements from the same ferrite sample material of thickness 0.15" under no magnetic bias. The two standing modes excited within the ferrite sample, say, the $\lambda/2$ resonances, occurred at lower frequencies, but showing approximately the same mode splitting in frequencies, please see Fig.12. This is because $4\pi M_s$ is the same but the thickness is now larger. When bias fields were applied, the changes in resonant frequencies are plotted in Fig.16 for bias under the permanent magnet only, the solid curve, and bias under the permanent magnet plus the Helmholtz coil, the dashed curve. The corresponding curves from calculations are shown in Fig.17. The magnetic linewidth used in the calculations of Fig.17 was $\Delta H = 1000$ Oe, which is larger than the quoted value of 200 Oe. This discrepance is due to the fact that the internal field is non-uniform within the ferrite sample, and the large $4\pi M_s$ and thickness of the sample result in an effective linewidth in the order of $4\pi M_s$. Calculations shown in Figs.11, 14 and 17 compared nicely with experiments, shown in Figs.12, 15, and 18, respectively.

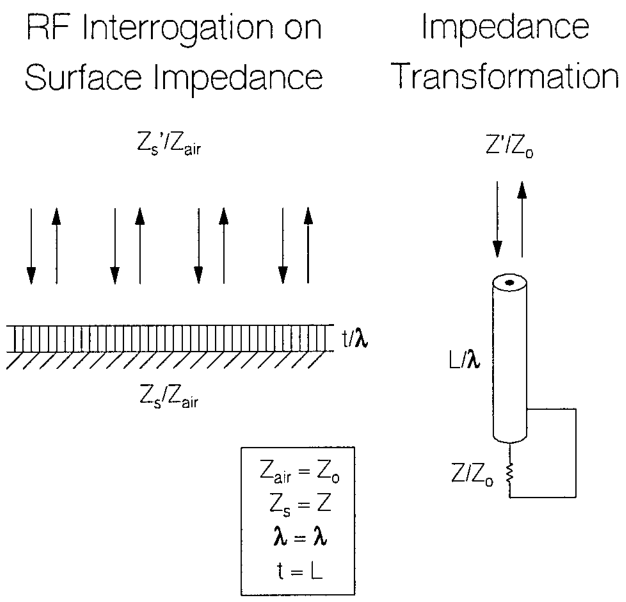

Fig.18 Analogy between surface-impedance interrogation in a boundary layer and in impedance transformation in a transmission-line segment.

PHASE CONTROL OVER ELECTROMAGNETIC SIGNAL

For an isotropic resonator showing circular symmetry, for example, an isotropic dielectric microstrip/stripline disk/ring resonator, the excited modes contain both clockwise and counterclockwise rotational modes, because these two modes are degenerate in frequency, and wave propagation is reciprocal with respect to rotation around the axial direction of the resonator. As such, phases are ambiguous if one attempts to couple out the excited modes of the resonator. This is no longer true for the operation of an anisotropic resonator in which the rotational symmetry of the resonator is removed. As a consequence, the two eigenmodes associated with clockwise and counterclockwise rotations of electromagnetic waves occur at different frequencies, and excitation of one mode excludes the other, and vise versa. This implies that the resonant modes are definite in phase, allowing the resonator to be effectively used as a phase shifter. In other words, the eigenmodes excited in a nonreciprocal resonator are traveling waves in nature, as in contrast to the standing eigenmodes excited in a conventional isotropic resonator supporting reciprocal propagation of electromagnetic waves.

Among many possible solutions in realizing our patented idea, explicit examples, or embodiments, are illustrated in this paper utilizing ferrite microstrip/stripline disk/ring resonators, since the design and fabrication of these kind of microwave circuits are well known. In a ferrite disk/ring resonator magnetized along the axial direction the degeneracy between the two counter-rotational modes is removed in the presence of an applied bias magnetic field, and the resonant frequencies of these two eigenmodes occur at different frequencies, denoted as f_+ and f_- for the clockwise and the counterclockwise rotational modes, respectively. While the operation of a ferrite junction circulator is designated at a frequency midway between these two frequencies, $f = (f_+ + f_-)/2$, circularly-polarized radiations are obtained from the disk/ring resonator if the excitation frequency is located near one of these two frequencies, f_+ or f_-. This implies that at resonance the resonant mode in a ferrite resonator showing circular symmetry consists of only one eigenmode whose phase can thus be determined without ambiguity.

This allows the resonant mode to be coupled out from the resonator with a definite phase, since only a single mode near f_+ or f_- is excited. Thus, by coupling out the resonant mode selectively from a sequence of positions of the resonator showing symmetry the output phase can be varied, but keeping the output amplitude at a rather constant level. In making this statement we have assumed the input position is fixed. The reverse also holds true. That is, by keeping the output position fixed, the output phase, but not the amplitude, can be varied if the input position is selectively changed from a sequence of positions showing symmetry, exciting the resonant mode with a definite phase. Since the operation is designed away from ferrimagnetic resonance (FMR), low insertion loss is thus assured. Note that a ferrite junction circulator, which makes use of the standing modes inside a ferrite resonator rather than the aforementioned traveling waves, has generally shown an insertion loss less than 0.5 dB, and an even smaller insertion loss, say less than 0.1 dB, can be obtained if the circulator operates over a narrow frequency band. This implies that phase shifts induced from a nonreciprocal resonator are potentially low insertion loss, if the coupling impedance has been well matched at the input/output ports.

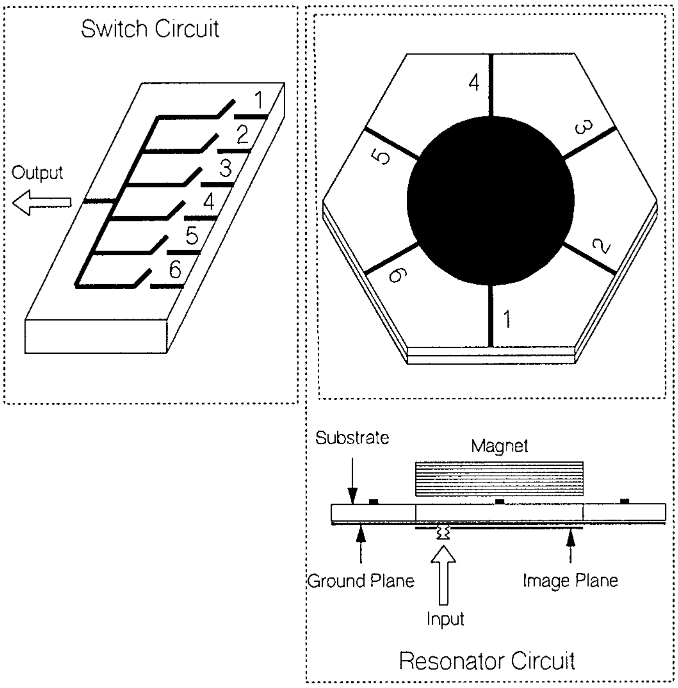

Fig.19 A first example of phase shifter using ferrite resonator.

A microstrip ferrite disk resonator is schematically shown in Fig.19, whose top view is shown at the top right and the side view at the bottom. A metal circular patch is deposited on top of the ferrite substrate which has 6 output ports extending from the periphery of the disk resonator, marked as ports 1, 2, 3, 4, 5, 6, respectively. The input port located under the disk connected to a coax launcher. A permanent magnet is placed atop the ferrite resonator to induce nonreciprocity in wave propagation thereby removing the mode degeneracy at resonance. A magnetic image plane is located under the disk resonator so as to condense the bias field on one hand and to make the bias field uniform along the axial direction on the other hand. The output ports are connected to the respective ports of the switch circuit shown at left of Fig.19. By closing one switch at one time the output phase from the resonator circuit of Fig.19 can be uniquely determined.

In the presence of a magnetic bias field the resonant mode inside the resonator excited at a frequency near, say, f_+ consists of only the clockwise rotational wave with definite phase. The relative phases of the 6 output ports shown in Fig.19 are thereof fixed, incremented sequentially by an amount of $\pi/3$ from port 1 to port 6. Here, we have assumed the fundamental mode. High-order angular modes are not excited within the resonator. Thus, by selectively closing a switch of the switch circuit of Fig.19 the output phase is also incremented by $\pi/3$ from port 1 to 6, sequentially. In this example the substrate has been shown to include two layers. One layer is ferrite, which induces the required mode splitting and hence resulting in non-reciprocity in wave propagation. A second layer may be needed so as to provide more control over the operation of the phase shifter. For example, high dielectric material may be used as the second layer so as to reduce the size of the resonator. This allows the resonator circuit to be miniaturized, thereby facilitating the fabrication of a large phased array system. Miniaturized phase shifters are needed by a large phased array system, since the available space is often limited by the system.

As mentioned, an output port is selected if a corresponding switch at the switch circuit of Fig.19 is closed. Depending on the purpose of application, the switch can be realized in different forms, including mechanical switches, optical switches, electronic switches, or electromechanical switches. A mechanical switch might be slow, but it is nevertheless cost effective. Electronic switches can be fabricated using semiconductor junctions located in close proximity to the resonator ports to be integrated with the other phased array elements. Micro-ElectroMechanical Switches (MEMSs) provide high isolation between ports. Optical/Superconducting switches are fast devices and a response time shorter than 1 nsec can be readily achieved.

In short an rf signal enters the phase shifter of Fig.19 through the input port of the disk resonator, undergoing non-reciprocal rotation introduced with the ferrite substrate material, to be selectively coupled out by the switch circuit of Fig.19. The output phase of the phase shifter can thus be varied in increments of $\pi/3$. Since the resonator geometry is the same for all of the output ports, operation of the phase shifter is uniform, being independent of the angle in phase shift. This is in contrast to the operation of a conventional phase shifter incorporating a transmission line. In order to obtain a large phase shifting angle, the length of the transmission line has to be increased, resulting in a large insertion loss; or, the permittivity/permeability values of the substrate material needs to be varied appreciably, giving rise to a large return loss. In both cases the operation of a conventional phase shifter is non-uniform, thereby requiring individual tuning for each of the fabricated devices, which translates into high fabrication costs.

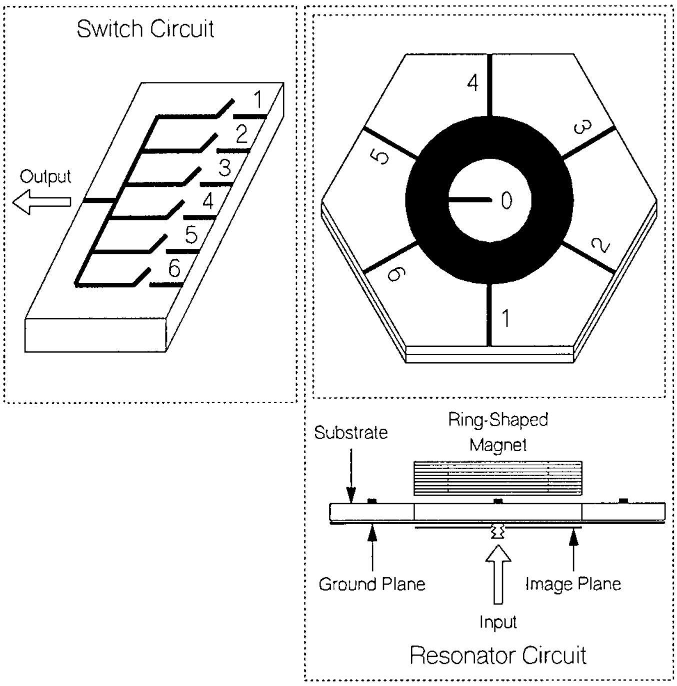

Fig.20 A second example of phase shifter using ferrite resonator.

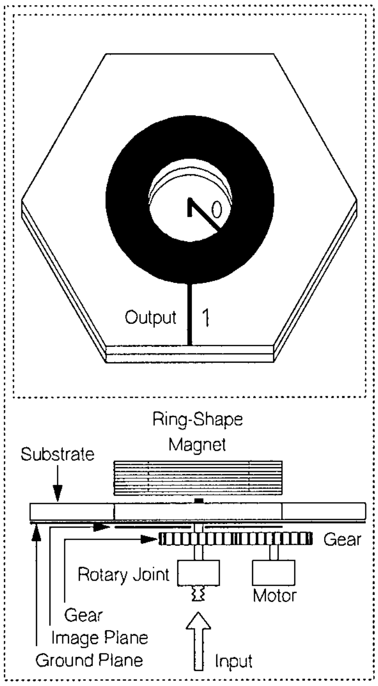

Fig.21 A second example of phase shifter using ferrite resonator.

The demonstration of Fig.19 includes 6 output ports. More output ports can be readily included without limitation. For example, by coupling out the resonator with N output ports feeding into a 1-pole N-throw switch-circuit, the output phase can thus be controlled in increments of 2/N. It is understood that the hexagon geometry assumed by the ferrite substrate depicted in Fig.19 is not necessary. For a resonator connected with N output ports the geometry of a regular N-vertex polygon may be assumed so as to warrant symmetry among the output ports. Or, a circular substrate can always be used regardless of the number of the output ports. The role of the input and the output ports shown in Fig.19 can be interchanged, and the input signal can appear at the pole port of the switch circuit; after closing a switch, the signal enters the resonator to be coupled out at the coax launcher with a definite phase.

Fig.20 shows a variation from Fig.19 in which a ring resonator is illustrated. In Fig.20 the input port, marked as port 0, feeds from the ring center connected to a coax launcher there, joining the ringresonator at the inner periphery. In biasing the ring resonator, a ring-shaped permanent magnet is used, placed above the resonator as shown in Fig.20. The rest of the circuit remains the same as shown in Fig.19 and discussions made with Fig.19 can be equally applied here.

Fig.21 shows a variation from Fig.20 where the input port, port 0, is replaced by a rotating arm using air as the substrate material. That is, a hole is drilled with the ferrite substrate which coincides with the central hole of the ring resonator, as shown in Fig.21. In Fig.21 port 0 is not fixed in position, and it is allowed to rotate around an axis located at the center of the ring resonator, contacting loosely, or coupling tightly to, the inner periphery of the ring patch of the conductor circuit of the resonator.

Air is used as the substrate material for port 0 so as to facilitate the mechanical motion of the rotating arm intended there.

The other end of port 0 is connected to the central conductor of a coax cable, which penetrates through the ground plane of the resonator from below, protruding into the hole region formed by the ferrite substrate, joining port 0 and making a 90° angle at the point of joint. This forms a rotating arm, consisting of port 0 and the central conductor of the coax cable, shaped as the letter "L" but upside down. Via a gear assembly, the coax cable, and hence the rotating arm , is loaded to a step motor which drives the rotating arm to perform rotational motion, as shown in Fig.21. A rotary joint is used to isolate the rotational motion of the coax cable from the coax launcher, which serves as the entrance for the input signal.

The operation of the phase shifter shown in Fig.21 is analogous to that shown in Fig.20 except that the input port has been changed from a stationary port into a rotating port, and the output port, denoted as port 1, has been fixed in position subject to no selection at all by imposing a switch circuit. In the presence of a bias magnetic field the degeneracy between the two counter rotational modes inside the ring resonator is removed, and when excited near one resonant mode, the other mode is suppressed, resulting in wave propagation with a definite phase.

Thus, the input signal feeds into the rotating coax cable, guided by port 0 and coupled to the ring resonator. Depending on the position of port 0 relative to port 1 phase shift is therefore uniquely determined. In contrast to examples shown in Figs.19 and 20, the phase shifter shown in Fig.21 involving a rotating arm eliminates the need for switches, and phase shift occurs at continuous angles. The roles of input and output shown in Fig.21 can be interchanged, and the resultant performance of the phase shifter is essentially the same. In Fig.21 more output ports can be added, connected to the outer periphery of the ring patch of the conductor circuit in a manner shown in Fig.20. For example, if 6 outputs are needed with their relative phases fixed differing by an amount of $\pi/3$ in sequence, one can employ a conductor circuit similar to that shown in Fig.20. This saves 5 phase shifters, if constructed separately each consisting of only one output port, as shown in Fig.21. Phase shifters providing multiple output phases are needed by a 2D steering phased array system.

A prototype phase shifter device whose schematic is shown in Fig.21 has been fabricated and characterized. The fabricated ferrite microstrip ring resonator used G1010 material (Trans-Tech, Adamstown, MD) characterized by the following parameters: saturation magnetization $4\pi M_s$= 1023 G, dielectric constant = 13.34, outer diameter OD = 0.85", inner diameter ID = 0.4", and thickness t = 0.05". The resonant frequencies of the fabricated ferrite resonator, or the modal chart, have been measured as a function of the bias magnetic field, which are shown in Fig.4. Calculations assuming perfect magnetic-wall boundary conditions are shown as solid curves in Fig.4, which compare reasonably well with measurements. Here the external magnetic field is assumed to be applied along the axial direction of the ring resonator. Three bias regions are distinguished in Fig.22, marked as Region I, II, and III, respectively. Region I denotes the unsaturated region, where the demagnetizing field cancels the applied field and only a fraction of the saturation magnetization is aligned by the external field. Region II denotes bias above FMR, Region III below FMR, and the FMR condition is marked by a dashed curve separating these two regions. For calculating the normal mode frequencies in the unsaturated region, or region I, we have assumed the magnetization of the ferrite substrate varies linearly with the external bias field

$$4\pi M = 4\pi M_s(H_o/H_s), \text{ for } 0 \leq H_o \leq H_s,$$

and H_s denotes the saturation field, a quantity strongly dependent on the demagnetizing factor of the resonator geometry, N_z. In Fig.22 we have fit the calculations with the measured resonant frequencies of the resonator, and the resultant saturation field was H_s = 800 Oe. This implies the demagnetizing factor $N_z \approx 0.78$.

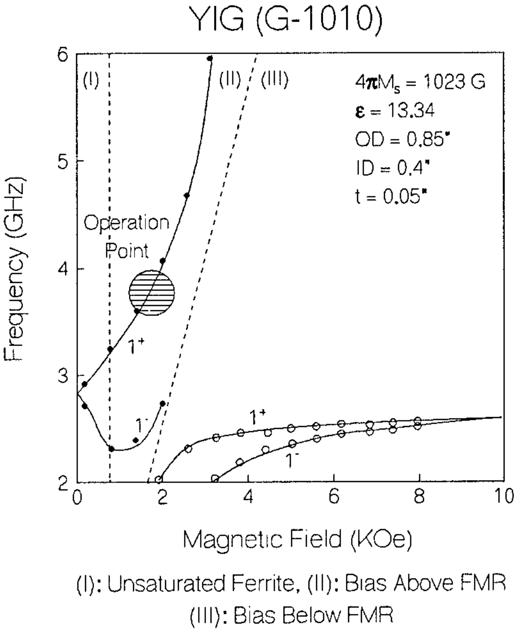

Fig.22 Measured and calculated dipole resonant frequencies of the fabricated ferrite resonator.

As shown in Fig.22 when the external field is zero, the so-called demagnetized state of the ferrite substrate, wave propagation is reciprocal, and hence the ferrite resonator behaves like a dielectric resonator for which the resonant frequencies of the two clockwise and counterclockwise rotational modes are degenerate. When the external bias field is increased above zero, the degeneracy between these two counter rotational modes are removed, and they assume different frequencies at resonance, as shown in Fig.4. When the bias field, H_0, far exceeds the saturation magnetization, $4\pi M_s$ and the operation frequency, f/γ, non-reciprocity is gradually reduced, and in this large bias-field limit wave propagation in ferrite becomes reciprocal again: the two counter rotational modes assumed by the resonator coincide in frequency as if they were propagating in a dielectric medium, as shown in Fig.22.

As revealed by Fig.22, the largest splitting between the two clockwise and counterclockwise rotational modes occur at ferrimagnetic resonance (FMR):

$$f = \sqrt{f_o(f_o + f_m)},$$

which describes a curve shown dashed in the modal chart of Fig.4, separating the two bias regions, Region II and Region III, corresponding to the bias above and below FMR conditions, respectively. Note that we have adopted the conventional terminology that bias above/below FMR refers to the applied frequency, but not the bias field, whose value is below/above the FMR condition. Although the FMR condition implies the largest modal splitting, it also means the largest magnetic loss, and hence its occurrence should be avoided for a practical device intended for transmission use, unless large attenuation is desired, such as in the applications of field limiters or absorbers. In measuring the resonant frequencies of the fabricated resonator circuit we have used an electromagnet to provide the bias magnetic field to remove the modal degeneracy. Also, the rotating arm coupler shown in Fig.21 has been removed to facilitate the resonator to be inserted between the electromagnet poles exploiting

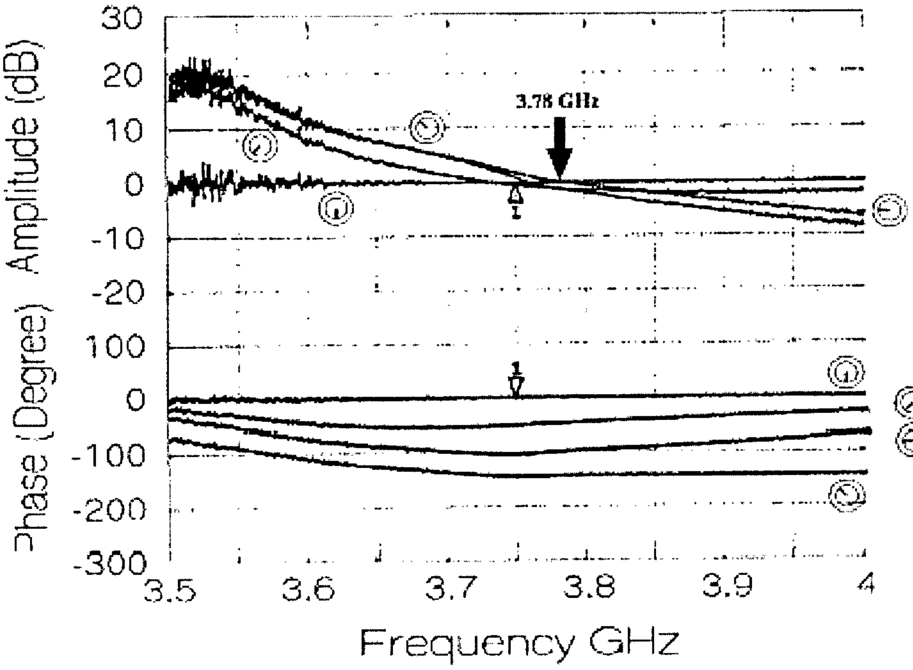

Fig.23 Measured amplitude and phase for rotation arm position from 0 to 180°.

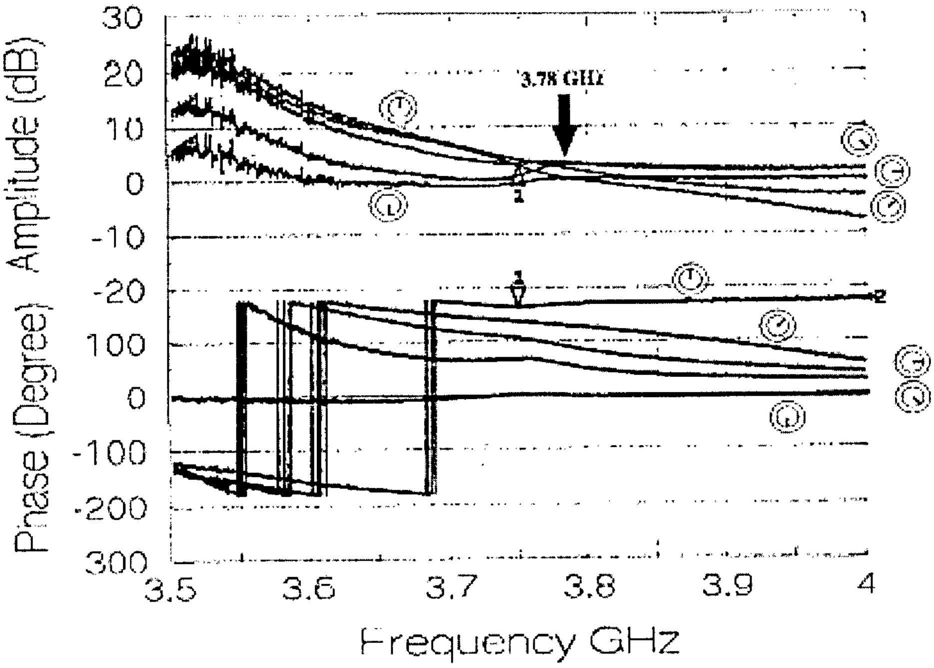

Fig.24 Measured amplitude and phase for rotation arm position from 180 to 360°.

a narrow air gap (< 0.5"). The dipole modal frequencies shown in Fig.4 were inferred from the reflection measurements, while treating the bias field as a parameter. High-order normal mode frequencies other than dipoles were also measured, which were not shown in Fig.22.

Figs.23 and 24 show the measured transmission phase and amplitude of the fabricated phase shifter. In biasing the ferrite resonator we have used a ring-shaped permanent magnet placed directly under the resonator. The magnet is samarium-cobalt, purchased from Texter, Woburn, MA, showing the following geometry: OD = 0.9", ID = 0.4", Thickness = 0.375". A magnetic image plane, or a permalloy foil cut into a ring-shaped geometry, was placed above the copper patch of the resonator, a microstrip cavity. The resultant bias field strength at the position of the ferrite resonator was measured to be 1050 Oe. As will be discussed shortly, the measured resonant frequency was near 3.78 GHz, implying the excitation of the dipole clockwise rotational mode in the ring resonator, or the 1^+ mode, as shown by a shaded circle in Fig.22. This resonant frequency agrees with calculations shown in Fig.22.

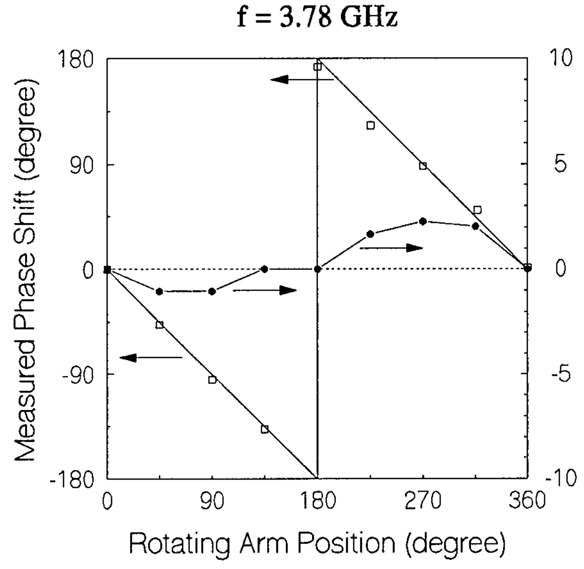

Fig.25 Transmission phase and amplitude of Fig.7 at resonant frequency are plotted as a function of rotating arm position.

The fabricated phase shifter is similar to that shown in Fig.21 except that the permanent bias magnet is placed under the resonator. We have used a rotary joint to isolate the rotational motion of the rotating arm from the input coax launcher. The rotary joint was purchased from Kevlin, Wilmington, MA, Model No. 1102H. A step motor was used to drive the rotating arm so as to induce a definite output phase. The DC motor was purchased from Colman Motor, Somerville, MA, type EYQM, which is characterized by the following parameters: Max Load Torque 1 oz-in, Max Load Speed 4500 rpm, Max Output Power 3.5W, and the Input Voltage 6 - 36 VDC. Transmission measurements were performed when the rotating arm was located, in reference to the output port orientation, at 0°, 45°, 90°, 135°, shown by Fig.23, and 180°, 225°, 270°, 315°, and 360°, shown by Fig.24. In Figs.23 and 624amplitude and phase measurements were normalized with respect to those values when the rotating arm was located at 0°, and the rotating arm position has been annotated numerically inside small circles affixed to the measured curves, top for the amplitude measurements and bottom for the phase measurements.

From Figs.23 and 24 it is seen that at the resonant frequency, f = 3.78 GHz, the transmission phase, which was originally 0°, decreased sequentially when the rotating arm was rotated away from 0°, passing across -180°, Fig.23, and then reaching -360°, Fig,24, when the rotating arm returned back to its initial position. Note that in Figs.23 and 24 the phase angle has been artificially added to (subtracted from) by 360° if it is less (more) than -/+180°, as commonly practiced by a phase plotter. The measured transmission phases, as well as amplitudes, are plotted in Fig.25 at the resonant frequency, as a function of the rotating arm position. From Fig.25 it is seen that the output phase of the phase shifter follows exactly the rotating arm position, as anticipated.

Note that in Fig.25, the measured transmission amplitudes of the phase shifter at the resonant frequency fluctuate slightly, about ±2 dB, due to manufacturing tolerances. On fabricating the rotating arm circuit inside the ferrite ring cavity the coax cable was bent away from its center position, resulting in the different coupling coefficients of the arm to the resonator at different rotational positions, maximal at the 0 and 180° positions, and minimal at the 90 and 270° positions. Hence, the insertion loss is a reflection of the coupling variations. The measured bandwidth of the phase shifter was, from the 3 dB insertion loss variation in Fig.23 and 24, slightly less than 5% of the center transmission frequency, as assumed by a typical reciprocal dielectric resonator. Note that a nonreciprocal resonator has a narrower bandwidth due to the non-degeneracy of wave propagation at the resonant frequency. The absolute minimum of the measured transmission loss at resonance was 0.33 dB occurred when the rotating arm was located at 0 and 180° positions.

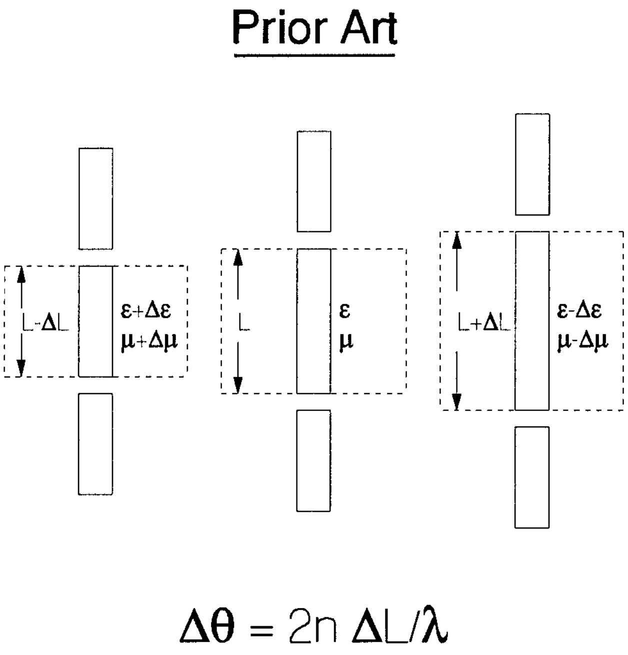

Fig.26 Conventional phase shifter utilizing a transmission line subject to electronic tuning.

Fig.26 shows the conventional approach that phase shifts are derived from a linear resonator supporting reciprocal wave propagation. As shown by the middle circuit of Fig.26 a linear resonator of length L is characterized by the two electronic parameters ∈ and μ, denoting the capacitance per unit length and inductance per unit length, respectively. If these two parameters are changed via, say, electronic means, the electrical length of the linear resonator will change accordingly, resulting in a shorter or a longer resonance length, corresponding to the increase of ∈ and μ to ∈+Δ∈ and/or μ+Δμ, shown at left of Fig.26, and the decrease of ∈ and μ to ∈-Δ∈ and/or μ-Δμ, shown at right of Fig.1, respectively. The derived angle in phase shift is

$$\Delta\theta = 2n\,\Delta L/\lambda,$$

where ΔL denotes the change in electrical length of the resonator, λ is the wavelength, and n is the order of resonance, for example n = 0.5 for half-wave resonance, and n = 1 for full-wall resonance, etc.. However, in

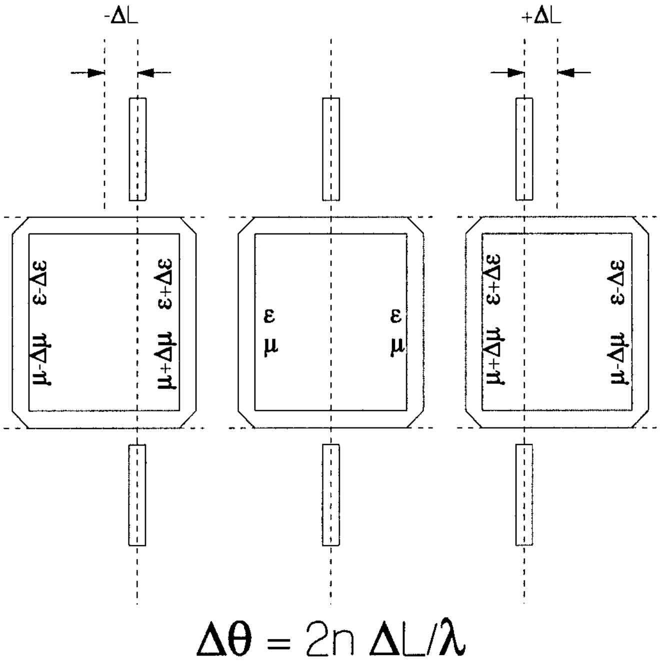

Fig.27 New circuit capable of obtaining balanced operation on phase shift.

accompanying the phase shift operation insertion loss is also changed, since wave propagation will experience different electrical lengths, resulting in different propagation losses, as shown in Fig.26. As such, the conventional circuit of Fig.26 is unbalanced and phase shifts thus obtained shows variations in insertion loss depending on the derived phase-shift angle. Amplifiers are thus needed by a conventional circuit to compensate for the non-uniform operation of the phase-shifter operation. The conventional approach is inconvenient and expensive.

Fig.27 explains how balanced phase shifts can be obtained from a resonator supporting nonreciprocal wave propagation. In contrast to the operation of a conventional linear resonator supporting reciprocal wave propagation, the resonance modes in a nonreciprocal resonator are non-degenerate allowing for phases to be unambiguously defined at specific positions As shown at the center of Fig.27 the resonator is divided in two equal parts showing symmetry which are loaded with electronically active materials characterized by the two electronic parameters ϵ and μ, denoting the capacitance per unit length and inductance per unit length, respectively. However, if these two electronic parameters are changed in a corporate manner so that one part counter reacts with the other, balanced operation results. This is shown in Fig.27, the left circuit, that ϵ and μ change to $\epsilon+\Delta\epsilon$ and/or $\mu+\Delta\mu$ for the left part and to $\epsilon-\Delta\epsilon$ and/or $\mu-\Delta\mu$ for the right part, leaving the overall electrical length of the resonator unchanged.. This results no change in the resonance condition, as in contrast to the left circuit of Fig.26. However, the coupling positions have been effectively changed from an electrical-length point of view, resulting in phase shift of an angle

$$\Delta\theta = 2n\ \Delta L/\lambda,$$

where ΔL denotes the change in electrical length of the resonator in these two respective parts, λ is the wavelength, and n is the order of resonance; for example n = 1 for the fundamental-mode resonance, and n = 2 for the second harmonic resonance, etc.. The prior art confirms this assertion, if the resonator supports nonreciprocal wave propagation. In other words, upon the change in electronic parameters the overall electrical length of the resonator remains unchanged, but rather the coupling positions of the feeders have been effectively shifted to the right from an electrical-length point of view..

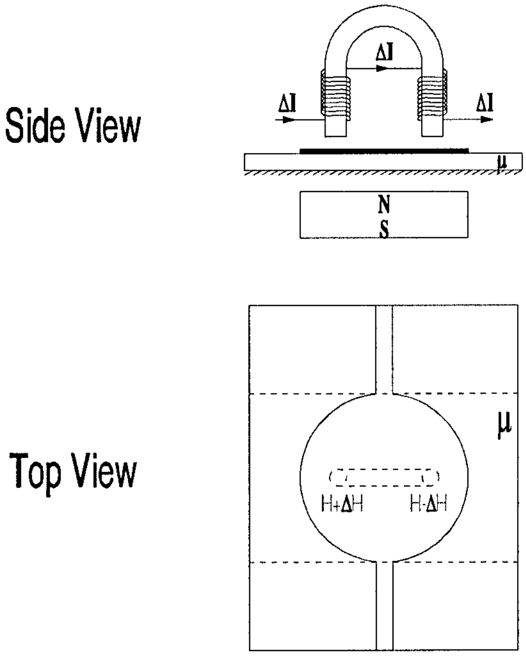

Fig.28 A variation from Fig.2 where the ring geometry has been replaced by that of a disk.

Analogously, the right circuit of Fig.27 shows the opposite process that ϵ and μ change to $\epsilon-\Delta\epsilon$ and/or $\mu-\Delta\mu$ for the right part and to $\epsilon+\Delta\epsilon$ and/or $\mu+\Delta\mu$ for the left part and the overall electrical length of the resonator is unchanged.. This causes the

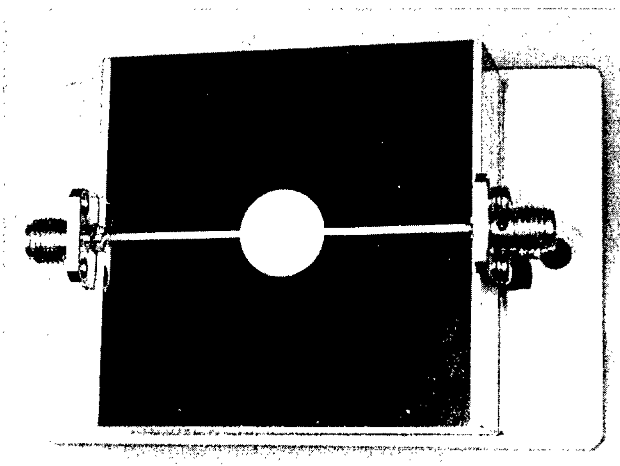

Fig.29 Fabricated phase shifter circuit involving a disk resonator on top of a ferrite substrate.

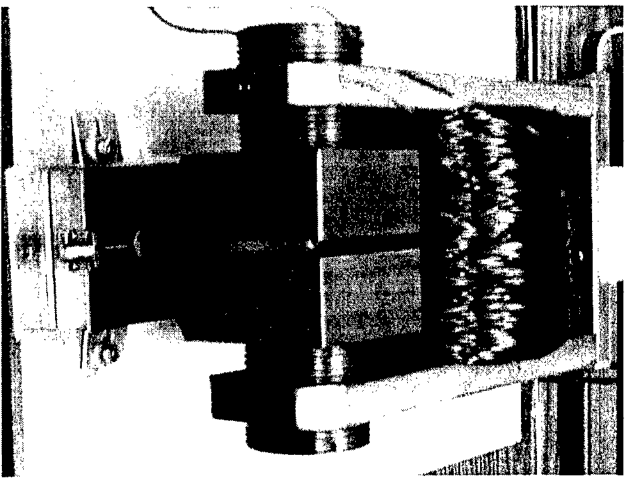

Fig.30 Fabricated electromagnet providing counter reacting fields onto the resonator circuit.

coupling positions of the feeders to effectively shift to the left, giving rise to phase shift of an angle

$$\Delta\theta = -2n\ \Delta L/\lambda.$$

Thus, the operation of the phase shifter device shown in Fig.27 is balanced, and the insertion/return loss will not vary with the phase-shift operation, to be valid to the first-order approximation, as in contrast to the conventional circuit of Fig.26. Amplifiers/isolators are thus no longer needed for the circuit of Fig.27, because the phase shifter entails the uniform operation. The ring geometry assumed by Fig.27 is not necessary, as shown by the disk geometry to be discussed with Fig.28. The ring resonator of Fig.27 can be realized incorporating the transmission-line geometries, including microstrip, stripline, waveguide, coax line, parallel wire, coplanar waveguide, image line, fin line, and slot line circuits, rendering convenience and versatility for device applications. As said, the electronic parameter ϵ and μ implied by the circuit of Fig.27 can be changed via electronic means, if the resonator is loaded with electronically active materials, such as ferrites, ferroelectrics, and/or varactors.

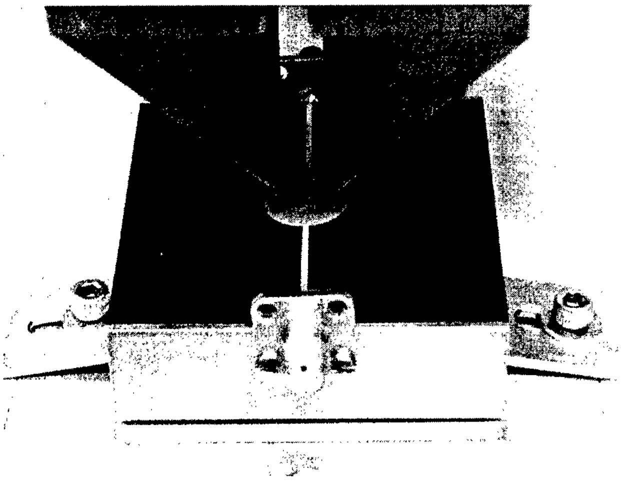

Fig.31 Detailed bias configuration.

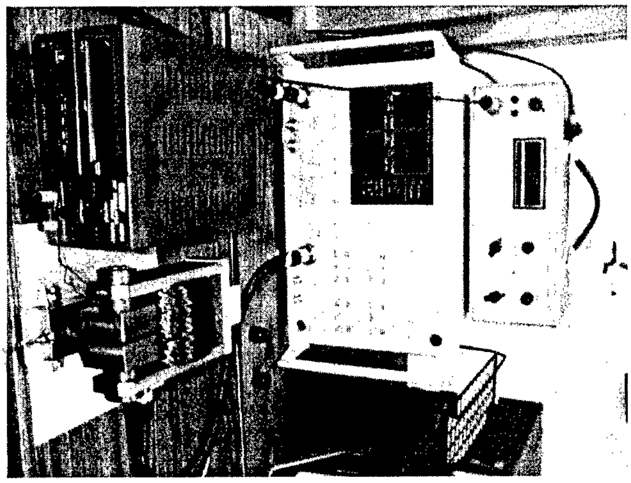

Fig.32 Measurement equipment setup.

Fig.28 shows another example of the balanced phase shifter circuit that a ferrite disk is biased by a constant magnetic field applied along the axial direction to stimulate nonreciprocal wave propagation. In Fig.28 the side view is shown at top and the top view is shown at bottom. The circuit shown in Fig.28 assumes the microstrip geometry and the substrate material includes a ferrite slab, denoted as μ in Fig.28. Ground plane is located under the ferrite substrate and the metal circuit is deposited atop the ferrite substrate. A permanent magnet is placed under the ground plane to generate a constant global magnetic bias so as to induce nonreciprocity in wave propagation in the ferrite disk region. A pair of balanced magnetic fields, called counter reacting fields, are applied onto the two sides of the disk resonator at symmetry, which are generated from two coils wound around a common yoke. The magnetic field generated by the permanent magnet is denoted as H and the magnetic field generated by the coil is denoted as ΔH, arising from the feed current ΔI. Thus, the right part of the disk resonator is biased by an effective total field of H+ΔH, and the left part by H-ΔH, causing the permeability value of the disk to change in a manner described with Fig.27. This results in balanced phase-shift operation, and the variation in insertion and return losses is thus insignificant. In Fig.28 the feeders assume to be coupled to the disk resonator conductively; other feeder coupling mechanisms are also possible, i.e., inductive coupling and capacitive coupling. The permanent magnet placed under the disk resonator can be replaced by an electromagnet. Or even better, hexaferrite (M-type self-biasing) materials can be included with the resonator substrate thereby eliminating the need for a common bias utilizing an external magnetic field.

T

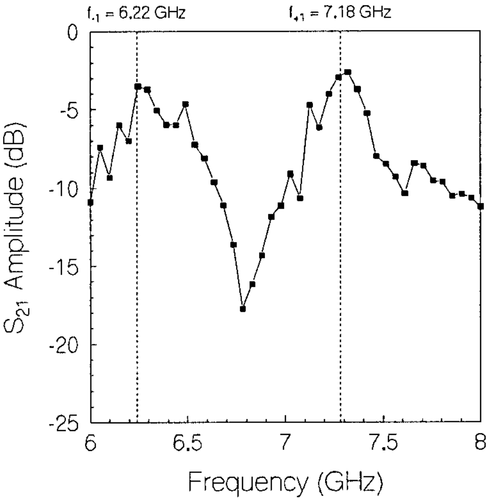

Fig.33 Measured transmission amplitude, which is insensitive to the bias magnetic field H_Δ.

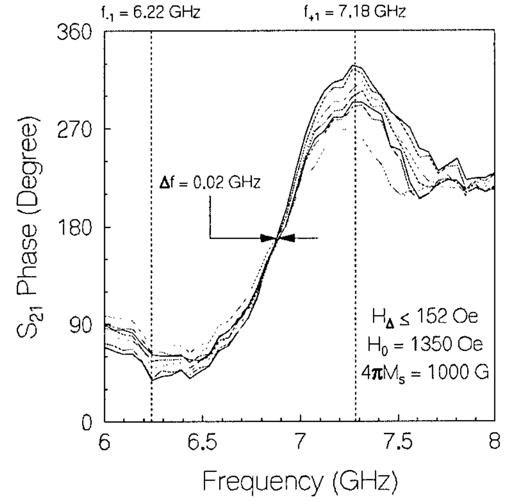

Fig. 34 Measured transmission phases as a function of the bias magnetic field H_Δ.

disk resonator circuit of Fig.28 has been fabricated, whose photograph is shown in Fig.29. The circuit consists of a microstrip disk resonator and the substrate is G1010 purchased from Trans-Tech, Adamstown, MD. The substrate is of a dimension 2"×2"×0.025" and the disk is of a diameter 0.45".

A Neodymium-Boron-Iron permanent magnet was placed under the disk resonator capable of generating a constant global magnetic bias of 1350 Oe, see Fig.28. The counter reactive bias fields were generated by an electromagnet placed above the disk resonator in a manner shown in Fig.28, see Fig.30. The yokes of the fabricated electromagnet have been tapered so as to facilitate the focus the bias fields into as small localized areas as possible, see Fig.31. The yokes were 0.025" above the disk resonator and the separation between the yokes was 0.18". The measurement equipments included a DC power supply, a Gauss meter, and a vector network analyzer, Anritzu 37369C, see Fig.32.

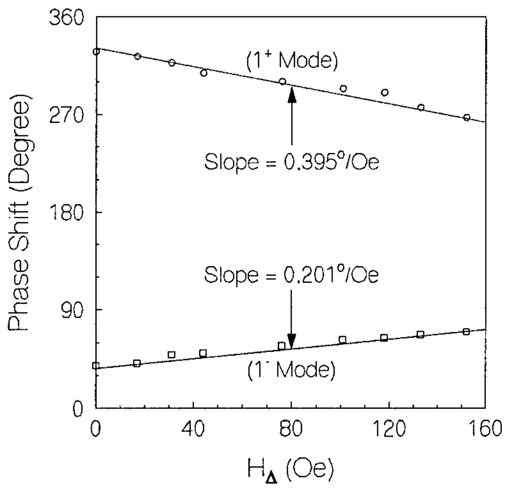

Fig.35 Phase tuning of the fabricated phase shifter shown in Fig.4.

The measured transmission amplitudes and phases are shown in Figs.33 and 34, respectively. Under the balanced condition the transmission amplitudes were insensitive to phase variations induced by the counter-reacting biasing magnetic field, H_Δ, and hence only a single amplitude trace is shown in Fig.33. However, the transmission phases were sensitively dependent on H_Δ, giving rise to a banded structure for their traces shown in Fig.34. In Figs.33 and 34 the plots were measured in the vicinities around the two counter-rotating dipole modes which are non-degenerate in their respective resonant frequencies: $f_{+1} = 7.18$ GHz, and $f_{-1} = 6.22$ GHz. When $H_\Delta = 0$, the transmission phases appear in Fig.33 as the outer most curve shown with the blue color. When H_Δ is gradually increased until $H_\Delta = 152$ Oe, transmission phases changes, to decrease for the +1 mode and to increase for the -1 mode. This functional dependence of $f_{\pm 1}$ on H_Δ is shown in Fig.35. From Fig.35 it is seen that the phase tuning range for the +1 mode is 61°, and for the -1 mode is 32°, giving rise to the phase tuning sensitivity of 0.395 and 0.201 °/Oe, respectively. The bandwidth of the ±1 modes is about 3% of their transmission frequencies, as indicated by the arrows located at the center of the transmission phase drawing, see Fig.9. We note that the balanced operation of the fabricated phase shifter device shown in Fig.4 is restricted to the region $0 \leq H_\Delta \leq 152$ Oe beyond which the resonant frequencies of $f_{\pm 1}$ will drift appreciably.

ELECTROMAGNETIC INTERROGATION INVOLVING HEXAGONAL FERRITE

Phase shifters are often constructed in terms of frequency-agile materials whose electronic properties can be changed via the application of a voltage or a magnetic field. While it is possible to fabricate a phase shifter at low frequencies by using a ferroelectric substrate, say, below 5 GHz, it is not very feasible if the frequency is increased to X-band or beyond, since ferroelectric materials are generally lossy at high frequencies. At X-band and above insertion losses are lower in ferrite substrates. By applying a bias magnetic field the effective permeability of a ferrite substrate can be continuously changed, resulting in variable phase shifts for microwave signals.

Difficulty in using a ferrite substrate is that the bias magnetic field is required to have a magnitude at least several thousand oersteds to effectively change the permeability of the substrate at X-band frequencies, for example. In order to reduce this bias-field requirement it is desirable to utilize the internal anisotropy field associated with a hexaferrite material to substitute, at least partially, the external field. In a ferrite material exhibiting hexagonal symmetry the internal crystalline anisotropy field can be as high as 50 KOe, admitting device applications even beyond 100 GHz. While self-biasing Y-junction circulators have already been demonstrated at Ka-band frequencies using M-type hexaferrite materials, the operation of a phase shifter fabricated with a Y-type hexaferrite is less understood. In this paper we present an analytical expression for the effective field appearing in a Y-type hexaferrite. The calculated transmission stopband compared almost exact with experiments, consisting of a microstrip line fabricated on top of a single-crystal Y-type hexaferrite substrate biased by a longitudinal field.

For a hexaferrite material crystalline anisotropy makes the magnetization direction along the c-axis energetically different from the directions lying on the ab-plane. For an M-type hexaferrite the c-axis is an easy axis, and the magnetization vector tends to be aligned along the c-axis even in the absence of an applied external field. In other words, in an M-type hexaferrite the crystalline anisotropy supplies an effective internal magnetic field along the c-axis capable of aligning the magnetization vector along that direction. Under small-signal approximation this effective anisotropy field behaves exactly as an externally supplied magnetic field viewed by microwave signals, and hence it may be utilized as a substitute for the external field. Important device applications for M-type hexaferrites include circulators and isolators, wherein the easy axes coincide with the thickness direction of the substrates so as to eliminate, at least partially, the bias-field requirement at high frequencies. The anisotropy field in an M-type hexaferrite can be measured using a vibrating sample magnetometer (VSM) for which the external bias field is applied in a direction transverse to the easy axis.

For a Y-type hexaferrite the c-axis turns out to be a magnetic hard axis and the magnetization vector tends to lie in the ab-plane in the absence of an applied magnetic field, and the ab-plane is termed an easy plane. In the past the effective field associated with an easy plane has been derived in a manner analogous to that following an easy axis. By doing so, however, the effective field for an easy plane depends on the direction of the magnetization vector, which defines the anisotropy contribution to the effective field and is conceptually different than a conventional external dc field. For example, the manner that an external field couples to the effective dc field of an easy plane is not specified. In this paper we develop an analytical expression for the effective field of a magnetic easy plane, stating that the effective field equals the geometric mean between the applied field and the sum of the applied field and the anisotropy field. This is in contrast to the effective field associated with a magnetic easy axis, which adds to the applied field arithmetically. Measurements shown below support this assertion.

Analogous to the M-type material, an effective anisotropy field can also be measured for a Y-type hexaferrite using the VSM technique for which the external bias field is applied normal to the easy plane. However, dissimilar to the M-type case, the measured anisotropy field can not be directly used

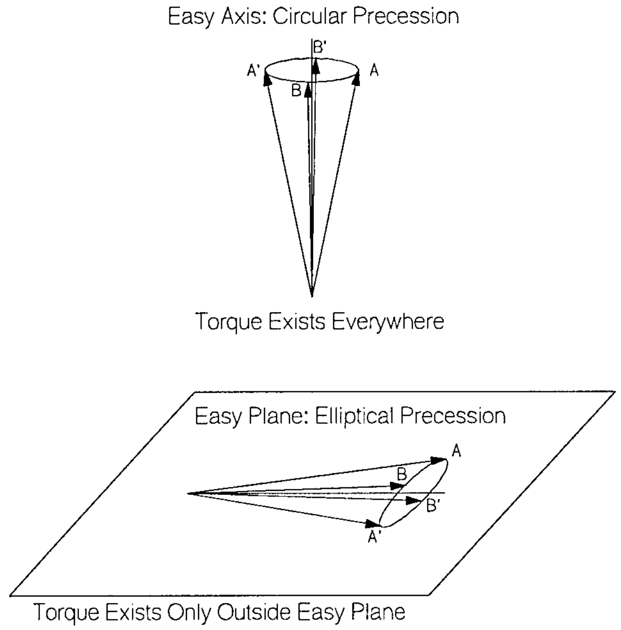

Fig. 36 Precessional motion of the magnetization vector around an easy axis (top) and an easy plane (bottom).

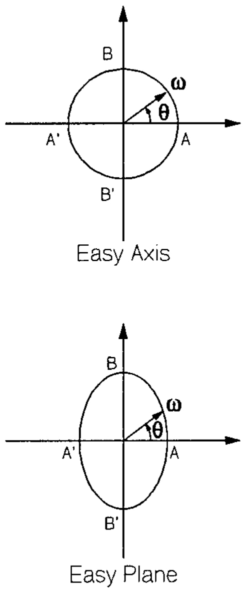

Fig.37 Polar plots of the angular velocity of the magnetization vector precessing around an easy axis (top) and an easy plane (bottom)

as the effective field for microwave signals. This is because when the magnetization vector is precessing around an internal field lying on the easy plane, the magnetization vector experiences no torque due to the anisotropy at the instant when it comes across the ab-plane; only when the magnetization vector precesses out of the ab-plane can the anisotropy field exert a torque. This is because the ab-plane represents an equal-potential surface for the anisotropy energy. Thus, the torque due to the anisotropy exerting on the magnetization vector is not uniform during its precessional motion, and the effective anisotropy field viewed by a microwave signal in a Y-type hexaferrite is smaller than is measured by VSM.

The precessional motion of the magnetization vector is depicted in Fig.36 for both cases of an easy axis (top) and an easy plane (bottom). For the case of an easy axis the magnetization vector undergoes a uniform precessional motion around the easy axis, experiencing a uniform torque exerted by the anisotropy, resulting in a constant angular velocity. This is shown in a polar plot at the top of Fig.37 where the loci of the angular velocity, ω, is a circle. However, for the case of an easy plane, the bottom of Fig.36, the precessional motion of the magnetization vector is not uniform. The anisotropy field exerts no torque at all on the magnetization vector at points A and A' lying on the easy plane, and a maximum torque is exerted by the anisotropy at the vertical positions labeled as B and B' at the bottom of Fig.36. Thus, in the presence of an easy plane the loci of the angular velocity traces out an ellipse, as shown at bottom of Fig.37, whose semi-major axis is

$$\omega_{max} = \gamma\ (H_o + H_A), \qquad (1)$$

and semi-minor axis is

$$\omega_{min} = \gamma\ H_o. \qquad (2)$$

Here, H_0 denotes the external field, H_A the anisotropy field measured by VSM, and γ is the gyromagnetic ratio.

The period of the non-uniform precessional motion is

$$T = \int_0^{2\pi} \frac{d\theta}{\omega}, \tag{3}$$

where θ denotes the precessing angle of the magnetization vector shown in Fig.37. Let this non-uniform magnetization-vector precession motion be associated with an effective internal field, H_i, whose Larmor frequency, γH_i, coincides with the period given by Eq.(3):

$$\gamma H_i = 2\pi/T. \tag{4}$$

We derive, therefore,

$$H_i = \left[\frac{\gamma}{2\pi} \int_0^{2\pi} \frac{d\theta}{\omega(\theta)} \right]^{-1}. \tag{5}$$

When the functional form of $\omega(\theta)$ is specified as an ellipse in the polar plot whose semi-major and semi-minor axes are given by Eqs.(1) and (2), respectively, we obtain, analytically, from Eq.(5),

$$H_i = [H_0 (H_0 + H_A)]^{1/2}. \tag{6}$$

Fig.38 shows how the anisotropy field H_A adds to the external field H_0 for both the cases of an easy axis and an easy plane. For a cubic material, or an isotropic material, the anisotropy field is insignificant comparing to H_0, and the magnetization vector undergoes a uniform precessional motion whose angular velocity is a constant, tracing out a circle of radius γH_0, denoted as ω_{min} in Eq.(2). For an easy axis pointing along the c-axis of an M-type hexaferrite, H_A adds to H_0 arithmetically, wherein the magnetization vector still undergoes a uniform precessional motion whose angular velocity traces out a circle of radius $\gamma (H_0 + H_A)$, denoted as ω_{max} in Eq.(1). However, for an easy plane coincident with the ab-plane of a Y-type hexaferrite, the magnetization vector no longer performs a uniform precessional motion, and the loci of the angular velocity

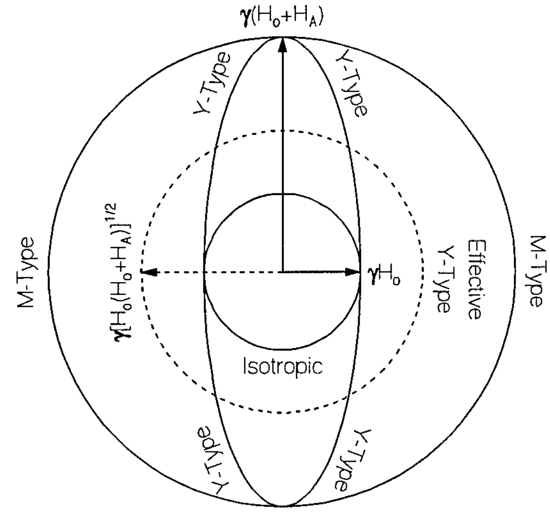

Fig. 38 Loci of the angular velocities for an isotropic material, an M-type hexaferrite, and a Y-type hexaferrite, and the construction of the effective internal field for the Y-type hexaferrite.

becomes, instead, an ellipse whose semi-major and semi-minor axes are ω_{max} and ω_{min} given by Eqs.(1) and (2), respectively. These three kinds of magnetization-vector precessional motions are shown as solid curves in Fig.38.

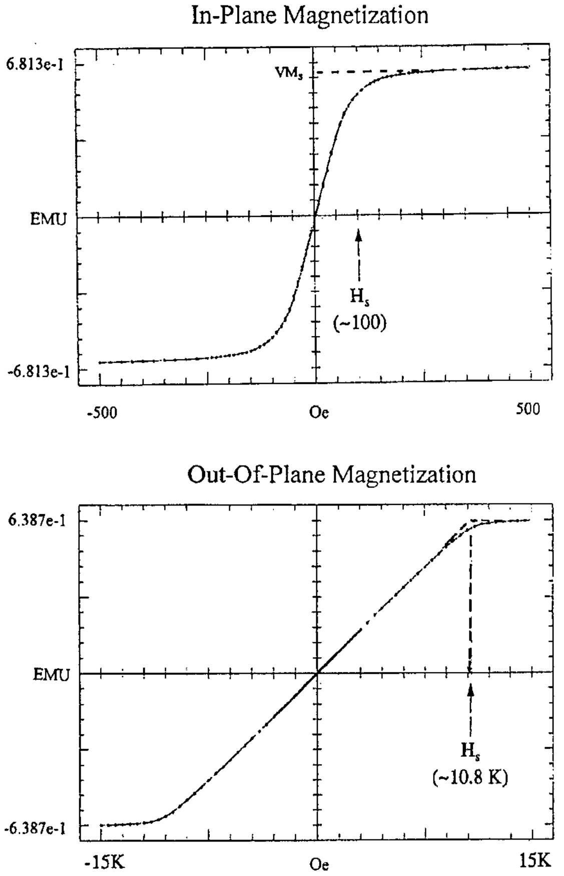

Fig.39 Measured VSM data of the Y-type hexaferrite substrate for in-plane (top) and out-of-plane (bottom) magnetization.

Now, Eq.(6) dictates that in the presence of an easy plane the magnetization vector can still be visualized as if it were performing a uniform precessional motion so long as the associated hypothetical motion is characterized by a Larmor frequency whose period is given by Eq.(3). This hypothetical motion is depicted in Fig.38 as a dashed circle whose radius is γ H_i, as specified by Eq.(6). This gives rise to an expression for the effective internal field H_i characteristic of an easy plane, Eq.(6). Note that H_i assumes a magnitude between the two fields corresponding to the isotropic case, H_0, and the case of an easy axis, $H_0 + H_A$. Actually, H_i appears as the geometric mean of these two fields, H_0 and $H_0 + H_A$, Eq.(6). In other words, H_i can be constructed in a geometrical manner that in Fig.3 a hypothetical circle is drawn whose area equals that of an ellipse representing the actual loci of the angular velocity. We note that in the above discussion we have assumed the other DC effective fields are zero, including the DC demagnetizing fields.[5] In case there are non-zero DC fields other than H_0, they need to be added to H_0 arithmetically before the construction of H_i giving rise to the total effective internal field in a Y-type hexaferrite possessing a magnetic easy plane. The effective field expression, Eq.(6), applies to wave propagation of arbitrary polarization, so long as the longitudinal component the magnetization vector does not couple into the precessional motion, as assumed by the small-signal approximation in deriving linearized equations of motion.

Thus, from Eq.(6), the internal field is increased, although not in a linear fashion, in the presence of an anisotropy field characteristic of an easy plane. Y-type hexaferrites are preferred to be used as the substrate materials for phase shifters at high frequencies, since then it is possible to eliminate the DC demagnetizing fields which would otherwise result if M-type substrates are used.

To verify our theory we have fabricated a microstrip transmission line using a single-crystal Y-type hexaferrite as the substrate material. The composition of the substrate material is $Ba_2MgZnFe_{12}O_{22}$, and the easy plane coincides with the substrate surfaces. The hexaferrite substrate material was characterized using a vibrating sample magnetometer (VSM) to show a saturation magnetization $4\pi M_S = 2.86$ KG, and an anisotropy field $H_A = 7.94$ KOe, as will be discussed shortly. These VSM data are shown in the top and the bottom diagrams of Fig.39, corresponding to the in-plane and the out-of-plane magnetization measurements, respectively.

It is seen in Fig.39 that the magnetization processes measured with the hexaferrite substrate material are indeed anisotropic. In Fig.39 the saturation force, H_s, has been increased by, roughly, two orders of magnitude when the hexaferrite material was magnetized along directions lying on the easy-plane, as shown in the top diagram of Fig.39, comparing to that when the material was magnetized toward a direction normal to the easy plane, the hard axis, as shown in the bottom diagram of Fig.39. In determining $4\pi M_s$ we have estimated the volume of the sample under VSM measurements, V, to be 2.802×10^{-3} cm^3, since the sample weight is 0.0153 g and the density is 5.46 g/cm^3. The value of VM_s is 0.64 emu, as shown in the top diagram of Fig.39. H_A is obtained as $H_s - 4\pi M_S$, where H_s denotes the measured out-of-plane saturation force shown in the bottom diagram of Fig.39, since the demagnetizing factor of the sample is roughly 1, assuming a thin-slab geometry for the sample.

The fabricated microstrip line is characterized by the following parameters: substrate thickness 0.010 inch, strip width 0.0051 inch, length 4 mm, dielectric constant 18, and the characteristic impedance of the microstrip line was designed to be 50 Ω. The width of the substrate is 4 mm. The external DC bias field was applied along the microstrip-line direction, giving rise to a negligible DC demagnetizing field. The measured transmission coefficients, in logarithmic scale, are shown in Figs.40a to 40c for the bias field H_0 equal to 0.5, 1.0, 2.5, 5.0, 7.5 and 10 KOe, respectively. As shown in Figs.40a to 40c, the characteristic impedance of the line is 50 Ω only at low frequencies away from ferromagnetic resonance (FMR), and the transmission intensity decreases when FMR is approached, forming a stopband, or a notch, in the FMR region.

In the FMR region the permeability of the substrate material varies abruptly from a very large positive value to a very small negative value, causing reflection of the incident wave (due to impedance mismatch) in addition to attenuation in wave propagation (due to magnetic loss). Thus, a stopband results, coincident with the region called the spin-wave manifold in the literature. In Figs.40a to 40c it is seen that the stopband moves upward in frequency as H_0 increases. This is shown in Fig.6 that the stopband, shown as vertical bars, increases monotonically with H_0. In Fig.41 the stopbands are defined at the 15 dB points of the measured notches in the transmission curves of Figs.40a to 40c, representing the FMR regions.

The effective permeability of the ferrite material may be expressed as

$$\mu_{eff} = 1 + \frac{\omega_m(\omega_m + \omega_i)}{\omega_i(\omega_m + \omega_i) - \omega^2} = \frac{(\omega_m + \omega_i)^2 - \omega^2}{\omega_i(\omega_M + \omega_i) - \omega^2}, \tag{7}$$

where

$$\omega_m = \gamma\, 4\pi M_s \tag{8}$$

$$\omega_i = \gamma\, H_i. \tag{9}$$

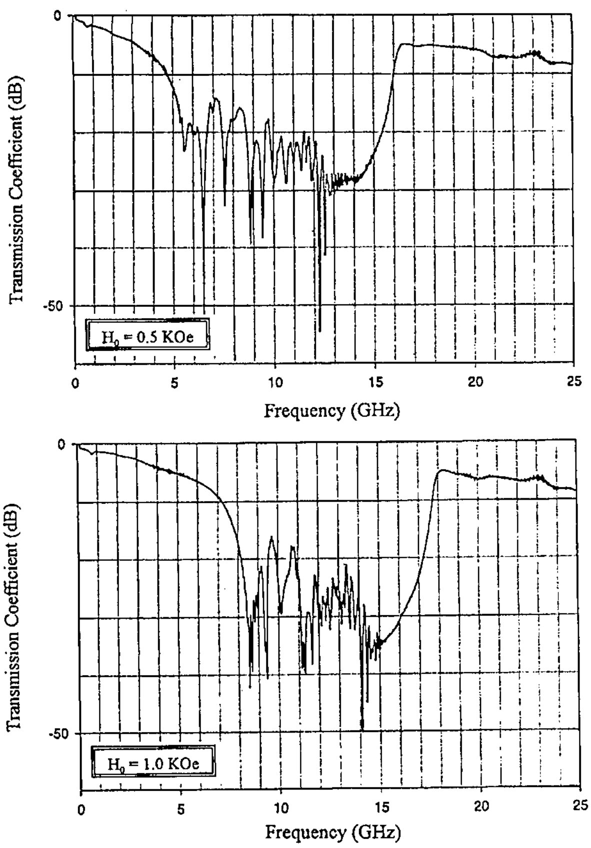

Fig. 40a Measured transmission data on Y-type hexaferrite substrate:H_o =0.5 KOe (top) and H_o = 1.0 KOe (bottom).

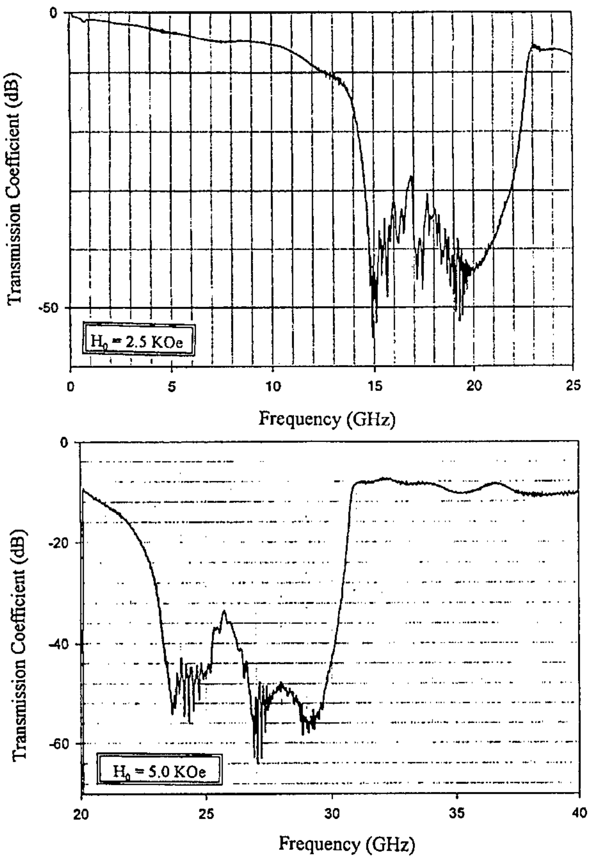

Fig. 40b Measured transmission data on Y-type hexaferrite substrate:H_o =2.5 KOe (top) and H_o = 5.0 KOe (bottom).

From Eq.(7) μ_{eff} is 0 and ∞ at the following two frequencies

$$\omega_{FMAR} = \gamma\ (4\pi M_s + H_i), \tag{10}$$

$$\omega_{FMR} = \gamma\ [H_i\ (4\pi M_s + H_i)]^{1/2}, \tag{11}$$

denoting the ferrimagnetic antiresonance (FMAR) and ferrimagnetic resonance (FMR) conditions, respectively. For $\omega_{FMR} < \omega < \omega_{FMAR}$ wave propagation is forbidden, since μ_{eff} is a negative number, implying evanescent modes rather than propagation modes. For $\omega_i < \omega < \omega_{FMR}$, μ_{eff} is a number appreciably larger than 1, resulting in reflection of the incident waves due to impedance mismatch. Thus, ω_{FMAR} and ω_i define the upper and lower bounds of the stopband of the transmission line. Note that ω_i is known as the Kittel frequency, and the stopband defined by ω_i and ω_{FMAR} coincides with the spin-wave manifold for an unbounded ferrite sample.

The stopband boundaries, ω_{FMAR} and ω_i, are shown as dashed curves in Fig.41, calculated from Eqs.(10) and (9) using Eq.(6) as the effective internal field, H_i. In Fig.41 the central solid line is calculated from using Eq.(11), denoting the FMR condition. From Fig.41 it is seen that calculations compare exact with measurements, implying that Eq.(6) is indeed a valid expression for the effective

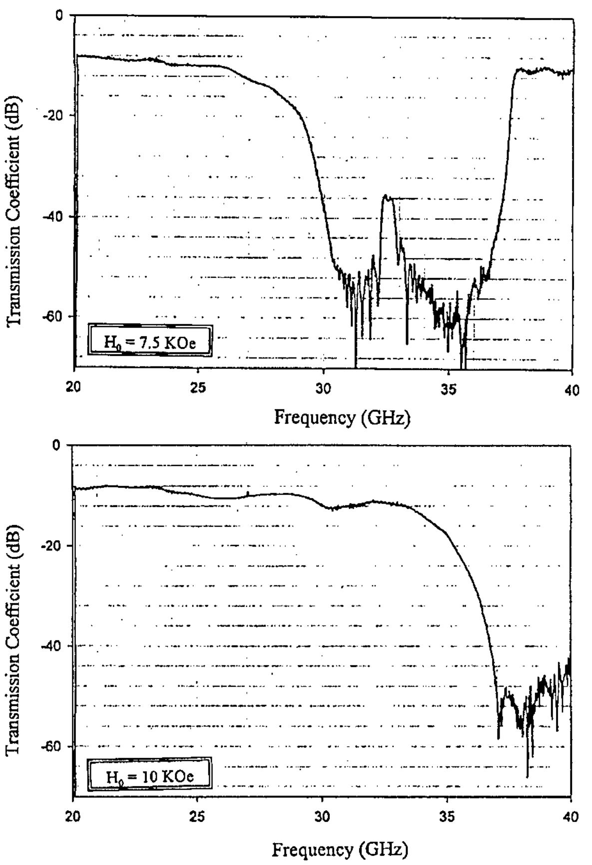

Fig. 40c Measured transmission data on Y-type hexaferrite substrate: H_0 =7.5 KOe (top) and H_0 = 10.0 KOe (bottom).

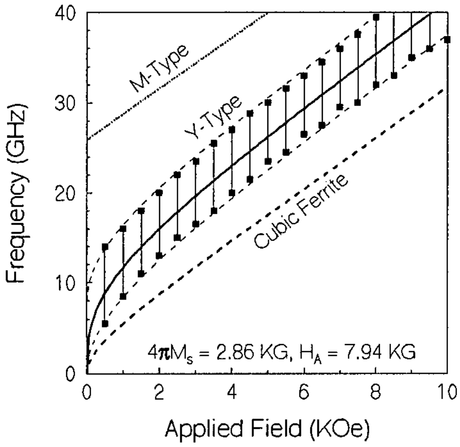

Fig. 41 Measured transmission stop-band, and other calculated frequencies, Eqs.(7) to (9), plotted as functions of the applied magnetic field.

internal field for a hexaferrite substrate possessing a magnetic easy plane. We note that in calculating ω_0, ω_{FMAR} and ω_{FMR} of Fig.41 we have assumed no adjustable parameters.

For completeness we also plot in Fig.41 the FMR curve corresponding to the case of a magnetic easy axis. This is shown in Fig.41 as the dotted line, where H_i is given by

$$H_i = H_A + H_0, \qquad (12)$$

which is used in Eq.(11). From Fig.41 it is seen that the anisotropy field behaves differently for an easy axis than for an easy plane, especially when H_0 is small. When H_0 goes to zero, the FMR frequency, and hence the transmission stopband, goes to zero accordingly for the case of an easy plane, whereas for an easy axis the FMR frequency remains finite when zero is approached by H_0. FMR curve for an isotropic ferrite is also plotted in Fig.6, shown as the lower heavy dashed curve, using Eq.(11) with $H_i = H_0$. Numerical calculations for wave propagation in the fabricated microstrip line have also been performed. We have adopted the transverse spectral-domain analysis to formulate a Green's function for the microstrip geometry involving a ferrite substrate. Current potentials have been used to construct the Galerkin elements, and calculations have been applied even in the stopband region. The calculated scattering parameters of the microstrip transmission line compared reasonably well with calculations.

PAST PUBLICATION

1. H. How, X. Zuo, E. Hokanson, and C. Vittoria, "Calculated and Measured Characteristics of a Microstrip Line Fabricated on a Y-Type Hexaferrite Substrate, IEEE Trans. Microwave Theory Tech., MTT-50(5), 1280-1288 (2002).
2. H. How, X. Zuo, and C. Vittoria, “Wave Propagation in Ferrite Involving Planar Anisotropy —Theory and Experiment” IEEE Trans. Magnetics, Mag-41(8), pp.2349-2355, 2005.
3. H. How and C. Vittoria, “Microwave Impedance Control Over A Ferroelectric Boundary Layer”, IEEE Trans. Microwave Theory Tech., MTT-52(9), pp.2177-2182, Sept. 2004.
4. H. How and C. Vittoria, “Microwave Impedance Control Over a Ferrite Boundary Layer” IEEE Trans. Magnetics, Mag-41(3), pp.1126-1131, 2005.
5. H. How and C. Vittoria, “Microwave Phase Shifter Utilizing Nonreciprocal Wave Propagation,” IEEE Trans. Microwave Theory Tech., MTT-52, 8, 2004.
6. H. How, “Balanced Microwave Phase Shifter,” submitted to IEEE Transactions, Microwave Theory Tech., February, 2006.

7 H. How, "Method and Apparatus of Obtaining Phase Shift Using Non-Reciprocal Resonator," Patent Number US 6,483,393, Nov. 19, 2002.

8. H. How, "Method and Apparatus of Obtaining Uniform Coupling from a Nonreciprocal Phase Shifter,” Patent Number US 6,963,254, Nov. 8, 2005.
9. H. How, "Method and Apparatus of Obtaining Balanced Phase Shift," Patent Number US 6,992,539, Jan. 31, 2006.
10. H. How, "Magnetic Microwave Devices," in "Encyclopedia of Electrical and Engineering," edited by J. G. Webster, vol.12, pp.31-45, John Wiley, 1999.
11. H. How and C. Vittoria, "Microstrip Antennas," in "Encyclopedia of Electrical and Engineering," edited by J. G. Webster, vol. Suppl. 1, pp.349-366, John Wiley, 2000.
12. H. How, "Magnetic Microwave Devices," in "Encyclopedia of RF and Microwave Engineering," edited by K. Chang, vol.3, pp.2425-2461, John Wiley, 2005.
13. H. How "Microstrip Antennas," in "Encyclopedia of RF and Microwave Engineering," edited by K. Chang, vol.3 pp.2580-2602, John Wiley, 2005.
14. H. How and C. Vittoria, "Surface Retarded Modes in Multilayered Structure: Parallel Magnetization," Phys. Rev. B., 39, 6823, 1989.
15. H. How and C. Vittoria, "Bulk and Surface Retarded Modes in Multilayered Structure: Anti-Parallel Magnetization," Phys. Rev. B., 39, 6831, 1989.